DIPLOMARBEIT

Dispersion analysis of an all-polarization-maintaining, nonlinear amplifying loop mirror, mode locked Ytterbium doped fiber laser

ausgeführt am

CD-Labor für Mid-IR Spektroskopie und Halbleiter Optik
der Universität Wien Fakultätszentrum für Nanostrukturforschung

unter der Leitung von

Univ.Prof. Dipl.-Phys. Dr.rer.nat. Thorsten Schumm

und

Dipl.-Phys. Dr. Oliver H. Heckl

eingereicht an der Technischen Universität Wien
Fakultät für Physik

durch

Wilfrid Grosinger
Matrikelnummer e0727219
Hohe Gasse 9
7441, Pilgersdorf, Österreich

Wien, im April 2020

Die approbierte gedruckte Originalversion dieser Diplomarbeit ist an der TU Wien Bibliothek verfügbar.
The approved original version of this thesis is available in print at TU Wien Bibliothek.
TU Bibliothek Your knowledge hub WIEN

Abstract

This master thesis presents the characterization of an Ytterbium-doped, all-polarisation-maintaining, nonlinear amplifying loop mirror mode-locked fiber laser, with a focus on dispersion-dependent mode-locking regimes. For this purpose, we built a mode-locked fiber laser based on a nonlinear amplifying loop mirror with nonreciprocal phase bias. The flexible design of the laser allowed us to operate the laser at different dispersion regimes. We used spatial wavelength separation and applying the technique of Knox for the net group delay dispersion (GDD) determination. We identified clean mod-locking states on a wide range of net cavity GDD. These states were further characterized by spectral shape, pump power, output powers, and their mode-locked behavior determined by the laser slope. Further than that, we demonstrated the reproducibility of the complete setup by rebuilding the laser and confirming that all pre-detected mode-locking states could be recreated.

Die approbierte gedruckte Originalversion dieser Diplomarbeit ist an der TU Wien Bibliothek verfügbar.
The approved original version of this thesis is available in print at TU Wien Bibliothek.
TU Bibliothek Your knowledge hub WIEN

Kurzfassung

In dieser Masterarbeit wird die Charakterisierung eines Ytterbium-dotierten, polarisationserhaltenden, nicht linear verstärkenden Faserschleifen-Spiegel vorgestellt. Bei der hier präsentierten Analyse wurde ein Schwerpunkt auf die Vermessung der unterschiedlichen dispersions-abhängigen modengekoppelten Regime gelegt. Zu diesem Zweck wurde ein modengekoppelter Faserlaser implementiert, der auf einem nicht linear verstärkenden Faserschleifen-Spiegel mit nicht-reziproker Phasenverschiebung basiert. Das flexible Design des hier vorgestellten Lasers erlaubte es, den Laser in verschiedenen Dispersionsregimen zu betreiben. Mit Hilfe der Technik von Knox wurden die Netto-Gruppenverzögerungsdispersion (GDD) der unterschiedlichen modengekoppelten Zustände vermessen. Der hier präsentierte Laser konnte über einen weiten Bereich der Netto -Gruppenverzögerungsdispersion (GDD) sauberer modengekoppelt werden. Verschiedene für die unterschiedlichen Dispersionsbereiche charakteristische Zustände wurden über die spektrale Form, Pumpleistung, Ausgangsleistungen, so wie die Laserkennlinie dokumentiert und charakterisiert. Darüber hinaus demonstrierten wir die Reproduzierbarkeit des Lasersystems, indem wir den Laser neu aufbauten und alle gefunden Modengekoppelten Zustände reproduzieren konnten.

Die approbierte gedruckte Originalversion dieser Diplomarbeit ist an der TU Wien Bibliothek verfügbar.
The approved original version of this thesis is available in print at TU Wien Bibliothek.
TU Bibliothek Your knowledge hub WIEN

Contents

1 Introduction 1

2 Theory 4
- 2.1 Ultra short pulses . . . 4
- 2.2 Ytterbium as a gain material . . . 5
- 2.3 Mode locked laser . . . 6
  - 2.3.1 Dispersion and self-phase modulation . . . 11
  - 2.3.2 Laser dynamics . . . 14
  - 2.3.3 Net-GDD . . . 18
  - 2.3.4 Laser components . . . 19

3 Experimental Setup and Methods 22

4 Results 27
- 4.1 Characteristic regimes . . . 28
  - 4.1.1 Negative net-GDD regime . . . 28
  - 4.1.2 Near-zero net-GDD regime . . . 31
  - 4.1.3 Positive net-GDD regime . . . 31
  - 4.1.4 Max positive net-GDD regime . . . 31
- 4.2 Laser slopes . . . 31
- 4.3 Knox-measurement . . . 37

5 Summary and Outlook 42

6 Appendix 44

7 Acknowledgments 45

Die approbierte gedruckte Originalversion dieser Diplomarbeit ist an der TU Wien Bibliothek verfügbar.
The approved original version of this thesis is available in print at TU Wien Bibliothek.
TU Bibliothek Your knowledge hub WIEN

1 Introduction

The constantly growing living standard of our society leads to ever increasing demands in areas such as manufacturing industry, automation, telecommunication, environmental science and health care. In all these fields, laser research makes important contributions. In the manufacturing industry, applications range from high-energy cutting and welding processes, up to precision lithography in semiconductor fabrication. In automation, industries benefit from cost reduction and increasing company productivity. In telecommunication, laser technology is necessary for high-quality data transfer. In environmental science, lasers improve general sample analysis like determining greenhouse gases in the atmosphere. In the health sector, laser technology is commonly applied to numerous medical fields, such as dentistry, cardiology, and neurosurgery. For example, lasers are used for eye corrections or tumor irradiation.
Since Albert Einstein outlined the basic laser operation principle [1] in 1917, by postulating the rate equations for absorption, and spontaneous and stimulated emission, the field of laser research has grown steadily. The first three-level device which used population inversion to generate a source of coherent radiation was the maser (microwave amplification by stimulated emission of radiation) [2], realized by Charles Hard Townes, James P. Gordon and Herbert J. Zeiger. Gordan Gloud coined the term "laser" (light amplification by stimulated emission of radiation) [3] for a similar device operating in the optical spectrum and mentioned applications in spectroscopy and interferometry. In the 1960s, Theodore H. Maiman demonstrated an pulse operating laser with a ruby crystal as the gain medium [4]. At the same time Ali Javan, William R. Bennett and Donald Herriott built the first continuous-wave (CW) laser by using helium and neon [5].
Nowadays lasers operate based on gaseous, liquid and solid gain materials. Furthermore, it depends on the application whether CW or pulse lasing is used. In the field of spectroscopy, further laser development initially focused mainly on building more and more stable CW lasers. In 2005, Theodor W. Hänsch and John Hall won the Nobel price for developing the so-called frequency comb [6], which is a specially stabilized pulsed laser with a discrete line spectrum. Since then, frequency combs have replaced CW lasers in many applications of spectroscopy due to the possibility for more accurate, more broadband and faster frequency measurements.
The line spectrum of a frequency comb [7] is discrete since the Fourier-series frequency representation of a pulsed laser produces an (almost) perfectly periodic train of identical pulses. The mechanism leading to such pulse formation is called mode-locking [8]. One distinguishes between active and passive mode-locking, where active mode-locking is based on an active modulator (like an acousto-optic or electro-optic modulator) to cause cavity losses. These losses are used to initiate mode-locking. On the other hand passive mode-locking is based on nonlinear effects, which cause high losses at low intensities

Die approbierte gedruckte Originalversion dieser Diplomarbeit ist an der TU Wien Bibliothek verfügbar.
The approved original version of this thesis is available in print at TU Wien Bibliothek.
TU Bibliothek Your knowledge hub WIEN

and low losses at high intensities in the laser. Passive mode-locking can be achieved by fast switching devices based on absorbing semiconductors or by indirectly exploiting other nonlinear effects. [9]. Currently, solid-state [10], fiber [11], wave-guide [12] and chip [13] lasers can generate mode-locking, but for wave-guide and chip lasers, output power scaling is difficult.

Laser applications are numerous due to the wide range of different laser properties. Solid-state lasers are characterized by relatively short resonator length and high repetition rate and thus, would in principle be well suited for spectroscopy. However, solid-state lasers are often rather sensitive to environmental perturbations. Additionally, some of their components are very specialized items and therefore expensive. An exemplary custom device used in solid-state lasers is the semiconductor saturable absorber mirror (SESAM) [14], which can be used for mode-locking. Another mode-locking mechanism uses Kerr lensing [15]. In Kerr lensing, to reach sufficient nonlinearity the intensity must be high and therefore the beam diameter must be small, which implies that the resonator is operated at the edge of stability. Hence, solid-state lasers are not the best choice for usage outside of research laboratories.

In contrast, fiber lasers are relatively insensitive to environmental perturbations due to strong light-guiding by total internal reflection in the fiber. This insensitivity enables the usage in field studies, e.g. mounted on drones. One application is the measurement of gas concentrations in the atmosphere, which is of great interest especially in times of global warming. Most of these gases have characteristic absorption lines in the mid-infrared (mid-IR) region. The mid-IR region is also called fingerprint region, which is named after the fact that in this spectral region molecules exhibit very characteristic absorption spectra that can be used as fingerprints for their identification. At the current state of research, only a handful of gain materials [16] for the direct generation of a mid-IR frequency comb have been reported. Moreover, the spectral coverage of those mid-IR frequency combs is limited and they sufficient average power. To overcome these problems, near-IR frequency combs are shifted into the mid-IR region via nonlinear frequency conversion [17].

One of the research goals of the Christian Doppler Laboratory for Mid-IR Spectroscopy in Vienna is to design and build a spectroscopy device, which is usable in the mid-IR and powerful enough to allow for Doppler-free absorption spectroscopy [18]. Such a system will be based on a near-IR seed laser which will be shifted to the 3 µm to 5 µm region while being tuneable over the full range. For high-accuracy measurements, the noise performance, the output power and the reproducibility of the generated frequency comb is of great importance. To satisfy all the properties listed above, a fiber laser system is chosen as seed laser because of its robustness and compactness. A further advantage of the system is the commercial availability of all required components. Fiber lasers based on nonlinear polarization rotation (NPR) [19] mode-locking are are one of the most frequently used, and have many practical applications. The physics of NPR mode-locked laser is well understood. However, a major disadvantage of NPR laser systems is the fact that they are usually not self-starting.

Recently, a new type of fiber laser with a mode-locking mechanism based on a nonlinear amplification loop mirror (NALM) [20] with a reciprocal phase bias, also known as

Die approbierte gedruckte Originalversion dieser Diplomarbeit ist an der TU Wien Bibliothek verfügbar.
The approved original version of this thesis is available in print at TU Wien Bibliothek.
TU Bibliothek Your knowledge hub WIEN

figure-9 laser [21], has been reported. The mode-locking mechanism utilized by figure-9 lasers enables the implementation of an all-polarization-maintaining (all-PM) fiber [22] laser design. The all-PM design makes them self-starting and even more insensitive to environmental perturbations. Mode-locked fiber lasers are well known to produce a large variety of different output properties such as spectral shape, output power, intra-cavity power, amplitude noise and phase noise depending on the net intra-cavity group delay dispersion (GDD) [23]. Performance properties of figure-9 lasers depending on the current intra-cavity GDD have not yet been studied. At the current state of research, the range of intra-cavity GDD in which stable mode-locking is possible is also not known. This master thesis discusses the different mode-locking states of figure-9 lasers with regard to the GDD. Furthermore, the reproducibility of the different operating states after rebuilding the setup is discussed. This master thesis is structured as follows. In Chapter 2, the theoretical aspects of the laser study are outlined. Chapter 3 shows the laser setup including the diagnostic setup and all experimental procedures. In Chapter 4, an analysis and discussion of the recorded data is presented.
Chapter 6 provides a summary of the MSc project and its main results. In addition, I discuss possible follow-up experiments that can be conducted on the basis of the work presented in this Master thesis in order to improve not only the understanding but also the performance of the laser type investigated here. The experiments and measurements presented here formed the basis for a journal article published in June 2020 [24].

Die approbierte gedruckte Originalversion dieser Diplomarbeit ist an der TU Wien Bibliothek verfügbar.
The approved original version of this thesis is available in print at TU Wien Bibliothek.
TU Bibliothek Your knowledge hub WIEN

2 Theory

2.1 Ultra short pulses

In general, a laser pulse train can be described as a superposition of sinusoidal waves having an ordered phase relation. The amplitudes, frequencies, and phase shifts of the sine waves determine the temporal and spectral shape of the pulse. The minimum pulse duration depends on the bandwidth of the entire spectrum. The fundamental modes result from the optical round trip length of the laser cavity. Due to chromatic dispersion inside the cavity, caused by the laser components, each frequency of the corresponding sinusoidal wave has a different optical path length. These optical path lengths result in non-equidistant frequency lines in the calculated cavity spectrum. However, the mode-locking mechanism forces the frequency lines to equidistant spacings. This can be most easily understood in the time domain: The mode-coupling process prefers to increase higher intensities, leading to a stable temporal pulse train with equidistant frequency spacing and an ordered phase relationship. Ordered phase relation means, in this context, there exists a time in the round trip, where the involved sinusoidal waves almost simultaneously interfere constructively.
The bandwidth of the frequency gain spectrum limits the pulse formation since the frequency lines outside the spectrum are not amplified, and therefore restrict the minimum pulse duration. This relation can be quantified via the time-bandwidth-product (TBP), which is the product of pulse duration Δt and the spectral width $\Delta\nu$, measured in full width at half-maximum (FWHM),

$$TBP = \Delta\nu\Delta t. \tag{2.1}$$

For each pulse shape there is a specific minimum TBP, defining the lower limit on the pulse duration for a given spectral bandwidth. Such optimally short pulses are called bandwidth-limited pulses or transform-limit pulses. If a pulse is guided through a transparent medium, the pulse interacts with its atoms, which influence the electric field. The influence on the carrier phase $\varphi(t)$ of the electric field leads to a time dependent instantaneous frequency ν_i, defined as

$$\nu_\mathrm{i}(t) = \frac{1}{2\pi}\frac{\partial\varphi(t)}{\partial t}. \tag{2.2}$$

If the instantaneous frequency is not constant, the temporal and spectral pulse shape change by transmission through a medium. The TBP of the so-called chirped pulse can change significantly compared to the TBP of the transform-limit pulse. The chirp will be discussed in detail in Sec. 2.3.1.

Die approbierte gedruckte Originalversion dieser Diplomarbeit ist an der TU Wien Bibliothek verfügbar.
The approved original version of this thesis is available in print at TU Wien Bibliothek.
TU Bibliothek Your knowledge hub WIEN

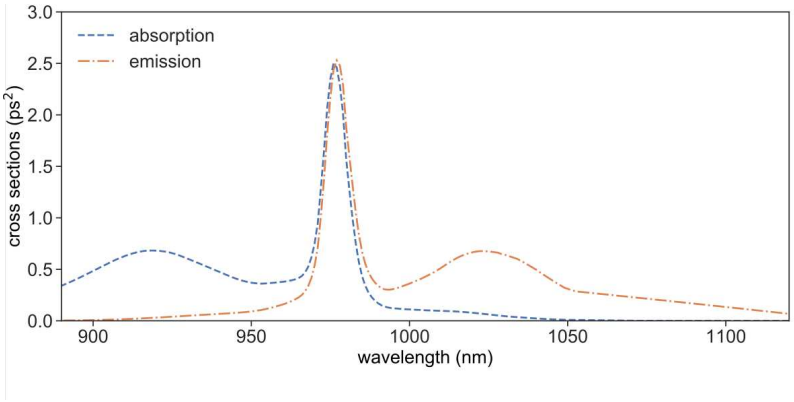

Figure 2.1: Effective absorption and emission cross-sections of Yb-doped germanosilicate glass.

2.2 Ytterbium as a gain material

As we have seen, a broadband gain spectrum is necessary to generate ultra-fast pulses. Ytterbium (Yb)-doped silica offers a broad gain bandwidth and is, therefore, an ideal gain medium for ultra-short pulse generation. Ytterbium works as a quasi three-level system, where the lower transition level is near the ground state. Since the lower transition level is close to the ground state, non-negligible reabsorption occurs. The reabsorption becomes less dominant at longer wavelengths, because the Yb behavior at longer wavelengths tends towards a four-level system. The reabsorption losses in the quasi three level wavelength region are accepted because a low quantum defect outweighs these disadvantages.
The quantum defect is defined as

$$q = h\nu_{\text{pump}} - h\nu_{\text{laser}}, \tag{2.3}$$

where $h\nu_{\text{pump}}$ is the pump energy and $h\nu_{\text{laser}}$ is the output energy of a single photon. The quantum defect is an essential value in laser design because a high q can lead to damage of the laser components by the dissipated energy.
The transition rate between two different energy levels is defined as

$$R = \sigma \frac{I}{h\nu}, \tag{2.4}$$

where σ is the transition cross-section, I is the intensity, and $h\nu$ is the photon energy. Due to the complexity of the possible energy sub-level transitions with their corresponding statistical weights, one usually works with effective absorption and emission cross-sections. These cross-sections also have the advantage that they are directly measurable and are easier to handle in laser modeling. Figure 2.1 shows the absorption and emission cross-section for the Yb-doped silica fiber that serves as gain material for this study. The fiber is pumped at 976 nm where the highest transmission rate into the 1030 nm region occurs.

Die approbierte gedruckte Originalversion dieser Diplomarbeit ist an der TU Wien Bibliothek verfügbar.
The approved original version of this thesis is available in print at TU Wien Bibliothek.
TU Bibliothek Your knowledge hub WIEN

2.3 Mode locked laser

Ultra-short pulse generation requires a mechanism called mode-locking that suppresses continuous wave (CW) lasing (low peak power) and improves pulse lasing (high peak power). The generation of femtosecond pulses requires a passive mode-locking mechanism since the limit for active mode-locking devices for pulse generation is in the picosecond regime.
Passive mode-locking arises from saturable absorbers based on absorption losses or artificial nonlinear phase shifts. A challenge for mode-locking of lasers is the generation of parasitic high energy giant pulses, also called Q-switch pulses. Such pulses are caused by temporarily high cavity losses due to the saturable absorber or misalignment of the cavity. Due to the missing cavity feedback, the gain material is pumped without any stimulated emission; hence all the pump energy is stored inside the gain material. By cavity loss reduction or spontaneous emission, a pulse with high energy and peak power is generated with much higher values than a standard pulse.
Therefore the precise design of the saturable absorber is of great importance. The semiconductor saturable absorber mirror, called SESAM [14], is based on absorption losses. The absorption of the mirror saturates for high intensity and therefore lets the pulses pass. A disadvantage of SESAMs is their difficult manufacturing procedure. In addition, small impurities and deviations from the absorber design shorten the lifetime or damage the device, which makes a SESAM unsuitable for the presented work.
Alternatively, artificial saturable absorbers can be realized, for example by exploiting the nonlinear phase shift of the Kerr effect in Kerr-lensing [15], nonlinear polarization rotation (NPR) [19] or in a nonlinear (amplifying) loop mirror [20]. The NPR laser, with its non-polarization-maintaining fiber, can only be used in a laboratory environment, since small environmental perturbations can cause polarization rotations. Uncontrolled polarization rotations harm the mode-locking, and thus the pulse will be unstable.
This problem can be solved by a mode-locking mechanism like a nonlinear optical loop mirror (NOLM), which can use a polarization-maintaining fiber. Figure 2.2a shows a nonlinear optical loop mirror (NOLM). The NOLM is a fast switching device with an X-coupler with connected port 3 and 4. In Fig. 2.2, the optical power is injected from only one port (e.g. port 1). If the fiber-coupler has a splitting ratio of 50:50, light injected at port 1 will be equally split into clockwise and counter-clockwise propagating light. In this case, there will be no phase shift for the two different propagation directions and interference at the coupler will lead to all light being redirected to input port 1, hence, the NOLM works like a mirror. If the splitting ratio is changed to a ratio unequal to 50:50, a phase shift between the counter-propagating waves will occur. The amount of the phase shift depends on the intensity, caused by the Kerr effect, which introduces an additional intensity-dependent refractive index. The resulting phase shift between the counter propagation waves changes the switching ratio from port 1 to port 2 by recombination of the pulses. The NOLM operates like an interferometric device, where the input power controls the switching behavior. Such behavior is exploited by ultrashort pulse formation.
The splitting ratio has a strong influence on the maximum transferred optical power

Die approbierte gedruckte Originalversion dieser Diplomarbeit ist an der TU Wien Bibliothek verfügbar.
The approved original version of this thesis is available in print at TU Wien Bibliothek.
TU Bibliothek Your knowledge hub WIEN

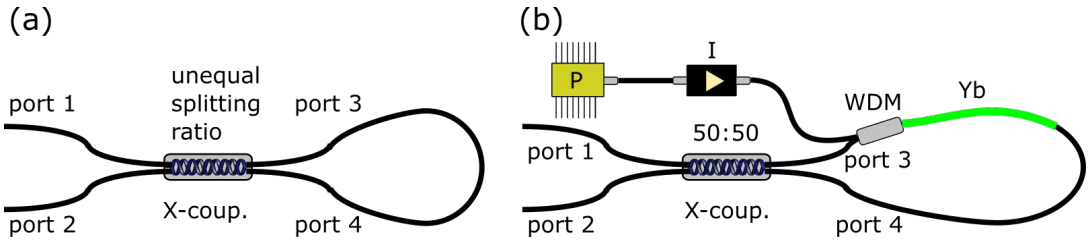

Figure 2.2: A basic configuration of a nonlinear optical loop mirror (NOLM) (a) and a nonlinear amplification loop mirror (NALM) (b), where X-coup is a ratio dependent X-coupler, WDM is a wavelength division multiplexer, I is a isolator, P is a pump diode and Yb is an Yb doped gain fiber.

between the ports. This ratio gives the modulation depth of the switching device. Nearly 100% of the light injected at port 1 is only transmitted at port 2 by a splitting ratio from almost 50:50. The periodic intensity-dependent switching behavior from port 1 to port 2 defines the transfer function for the NOLM, which also includes the modulation depth. The pulse transformation during propagation of the switching device should be low, and therefore similar to soliton transmission through an anomalous dispersion fiber ([20]). If this condition is fulfilled, the device will also have a good modulation depth. However, with a splitting ratio close to 50:50, high peak power is needed to get a sufficiently high phase shift between the clockwise and counter-clockwise propagating light. Therefore, the aim was to improve the NOLM.

The implementation of an amplifier inside the fiber loop and the use of an exact 50:50 splitter reduces the necessary peak power, while still offering full modulation depth. The amplifier is asymmetrically spliced into the fiber loop mirror, so that the counter-propagating waves have significantly different average intensities over the full path length and, therefore experience vastly different influence of nonlinear effects in the fiber path. This modified NOLM is called a NALM and shown in Fig. 2.2b. Spectral broadening through self-phase modulation (SPM) occurs via nonlinear amplification. This can be mitigated by anomalous GDD [25]. A typically used silica fiber has a zero-dispersion wavelength of around 1.3 µm and is therefore used in an Erbium laser (emission wavelength of 1.5 µm) as an anomalous dispersion fiber. In contrast, in Yb lasers with a zero-dispersion wavelength of around 1.6 µm, the fiber works as a normal dispersion fiber. The balance of dispersion and SPM in the NALM made it possible to build an all-fiber laser with Erbium as the gain material. Figure 2.3 shows this laser, which is called Figure 8 laser. The Erbium figure-8 laser is a good example for a common laser design based on the NALM principle. One extended the NALM by an external loop (connect port 1 with port 2) containing an optical isolator. The isolator blocks the external loop in the direction in which the NALM operates in CW laser mode, which occurs with no relative phase shift between the counterclockwise propagating pulses. The isolator is permeable in the direction in which the NALM produces a relative phase shift at higher intensities and thus letting the whole system act as a saturable absorber and supporting pulse formation. As mentioned above, the transfer function of the NALM interferometer

Die approbierte gedruckte Originalversion dieser Diplomarbeit ist an der TU Wien Bibliothek verfügbar.
The approved original version of this thesis is available in print at TU Wien Bibliothek.
TU Bibliothek Your knowledge hub WIEN

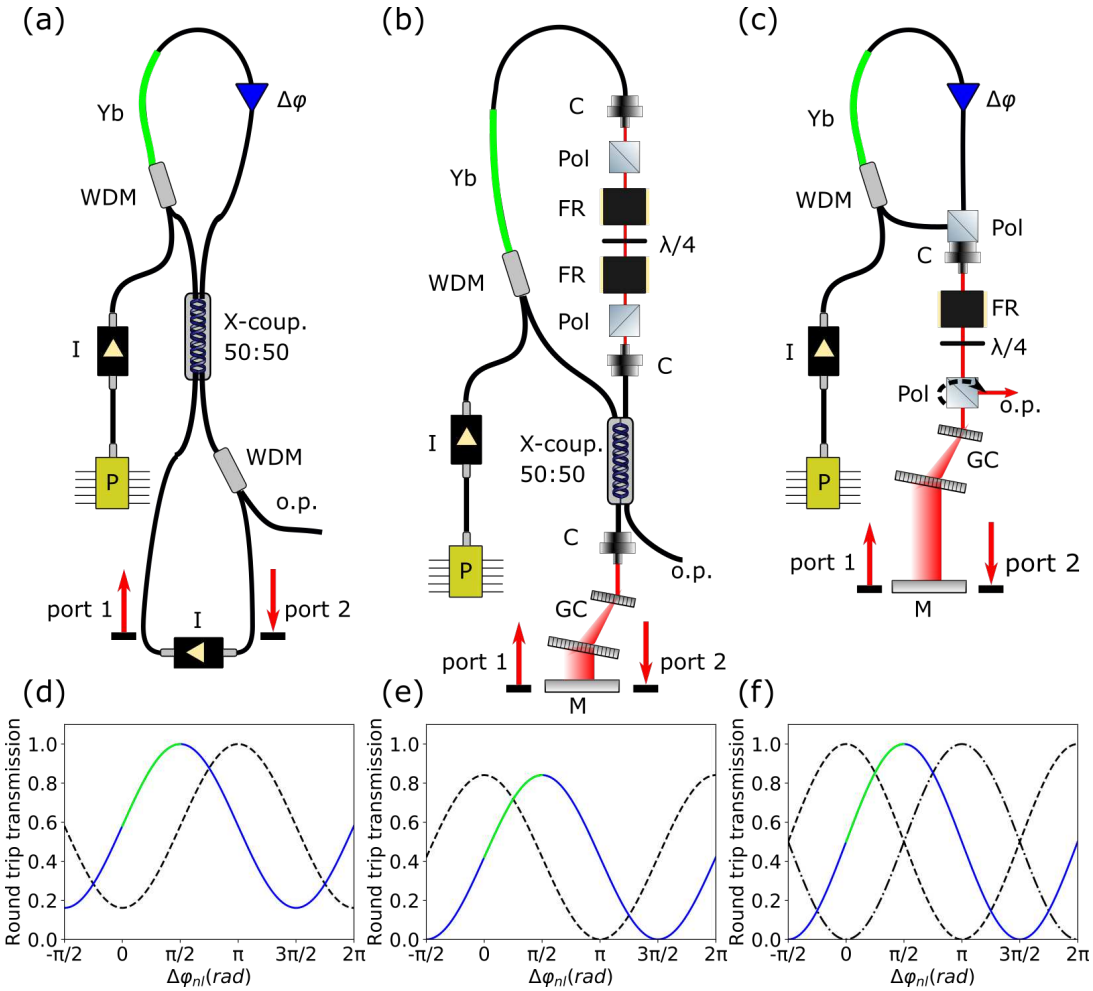

Figure 2.3: Schematic sketches of three different passively mode-locked laser setups and their respective transfer functions. A figure-8 laser with an isolator in the external loop (a), a figure-9 laser with an X-coupler where the nonreciprocal phase bias occurs in the NALM (b), a figure-9 laser with a polarization-dependent beam splitter where the nonreciprocal phase bias occurs outside of the NALM (c). In the schematic sketches, WDM is a wavelength division multiplexer, X-coup. is a ratio-dependent X-coupler, I is an isolator, P the pump diode, $\Delta\varphi$ is an additional phase bias device, C is a collimator, Pol. is a polarization dependent beam splitter, FR is a Faraday rotator, GC is a grating compressor, M is a mirror, $\lambda/4$ is the corresponding waveplate, Yb is the Yb doped gain fiber and o.p. is the output port. The respective transfer functions of the three laser designs are shown in (d), (e) and (f), where the dashed line shows the transfer function without an additional phase bias and the blue line with additional phase bias. The green line shows the optimal position for mode-locking. The dot-dashed line in (f) shows the transfer function with rotated polarizer.

Die approbierte gedruckte Originalversion dieser Diplomarbeit ist an der TU Wien Bibliothek verfügbar.
The approved original version of this thesis is available in print at TU Wien Bibliothek.
TU Bibliothek Your knowledge hub WIEN

shows the transmission from port 1 to port 2 corresponding to the relative nonlinear phase shift between the two counterpropagating waves in the NALM ring. An initial intensity fluctuation through laser gain pumping and the positive slope of the transfer function of the figure-8 laser (see bottom panel of Fig. 2.3a) leads to pulse formation by mode-locking. An additional nonreciprocal phase bias device shifts the transfer function so that the maximum of the transfer function occurs with a smaller relative phase shift. This improves the self-starting behavior because of the faster response due to a larger gradient of the transfer function. Further, the transfer function shows the full modulation depth at lower optical power. The figure-8 laser without phase bias has, by design, a positive gradient of the transfer function. Therefore, a phase bias device is not necessary for mode-locking.

One application for a figure-8 laser is as a frequency comb for metrology or high-resolution spectroscopy applications, which requires high stability and low noise. In such applications, a high repetition rate ($f_{\mathrm{rep}} > 150\,\mathrm{MHz}$) is often needed. Replacing the external loop with a linear free-space-arm, which significantly reduces the resonator length, solves the problem of achieving a higher repetition rate. In this setup port 1 is also used as port 2, except for the opposite direction of propagation, i.e. port 2 is the output from the input of port 1 after interaction with the NALM. This configuration additionally allows a f_{rep} stabilization via translation of the end mirror.

A disadvantage associated with the free space part is the possibility of harmful giant pulses, also called Q-switch pulses, discussed in Sec. 2.3.

However, the advantages of these extensions prevail and lead to the so-called figure-9 laser, named like that because of the experimental setup, which vaguely resembles the figure of nine as can be seen in Figs. 2.3b and c.

These extensions lead to the so-called figure-9 laser, named like that because the experimental setup vaguely resembles a figure of nine as can be seen in Fig. 2.3b and c. For figure-9 lasers based on a Yb gain material, there is no standard fiber with anomalous dispersion in the required wavelength range available. Therefore, a grating compressor is added in the free space section for dispersion compensation. The transfer function of this laser shows a negative gradient initially. An additional nonreciprocal phase bias device shifts the transfer function in such a way that a positive gradient results. The phase bias device consists of two Faraday rotators and a $\lambda/4$-waveplate in between. The Faraday rotators tilt the counter-propagating waves such that the $\lambda/4$-waveplate produces a phase delay in only one direction. After that, the electromagnetic field rotates back to the slow axis of the fiber. Two additional polarizers are added in front of the polarization maintaining fibers. The polarizers eliminate the amplified spontaneous emission (ASE) in the slow axis of the polarization-maintaining fiber. The polarizer blocks the fast axis of the polarization-maintaining fiber and allows only for lasing in the slow axis.

An additional modification of the figure-9 laser has been reported by Hänsel et al. [21]. In their setup, a polarization-dependent beam splitter replaces the 50:50 optical X-coupler, which allows a flexible adaptation of the phase bias and the modulation depth. The NALM in this configuration consist of the $\lambda/4$-waveplate, the Faraday rotator, polarizer with collimators, and the NALM loop ends at the outcoupling polarizer. The transfer function is defined as the ratio between port 1 and port 2, which can be defined in this

Die approbierte gedruckte Originalversion dieser Diplomarbeit ist an der TU Wien Bibliothek verfügbar.
The approved original version of this thesis is available in print at TU Wien Bibliothek.
TU Bibliothek Your knowledge hub WIEN

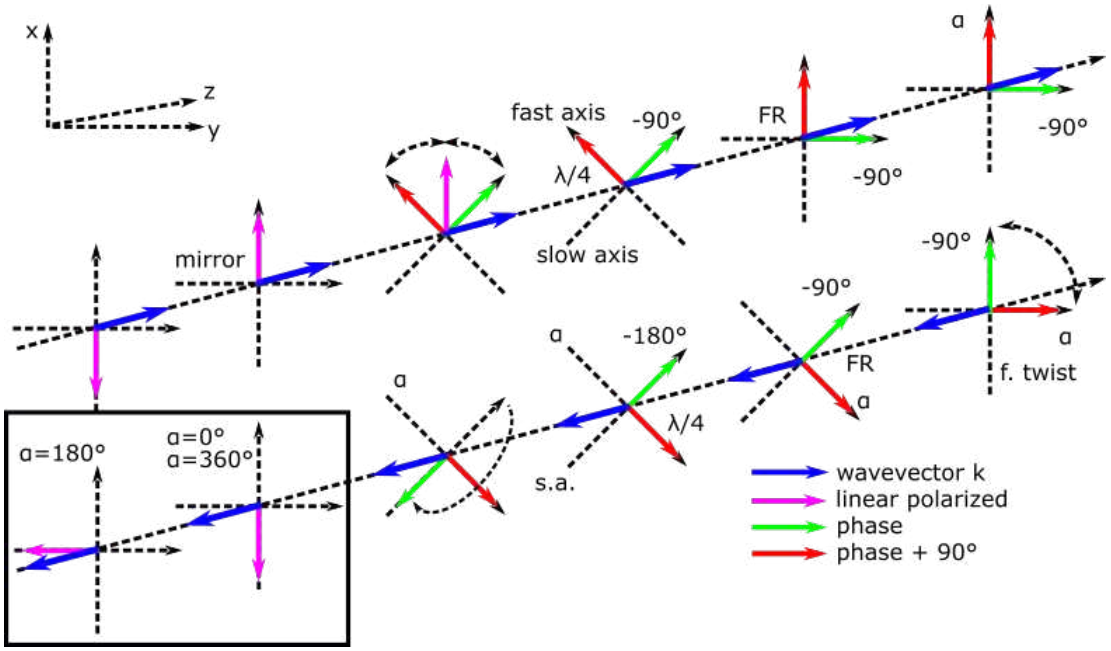

Figure 2.4: Schematic sketch of the polarization propagation through an ideal figure-9 laser starting after the polarization beam splitter. The sequence starts with the mirror, followed by the $\lambda/4$-waveplate, the Faraday rotator, and the twisted polarization-maintaining fiber. On the return way, the FR, the $\lambda/4$-waveplate, and the polarization beam splitter are passed again.

setup below the out-coupling polarizer, see Fig. 2.3f. In the reported configuration, the phase bias occurs in the free space section enabling a more compact setup. To omit one of the free space parts improves the vulnerability to environmental disturbances.
Figure 2.4 shows the ideal switching process, which leads to the mode-locking. Starting with a linearly polarized wave after the polarizer, the $\lambda/4$-waveplate causes a 90° phase delay on the slow axis. Polarization rotation by the FR and a 90° fiber twist change the polarization such that the second pass of the $\lambda/4$-waveplate also adds a phase shift on the same axis as before. This 180° nonreciprocal phase bias leads to the transfer function shown in the bottom panel of Fig. 2.3c. The transfer function does not support pulse formation since the transmission decreases with increasing SPM. Therefore, the out-coupling polarizer is rotated by 45°, shifting the transfer function such that a smaller relative phase shift is required. With a further phase bias device, the transfer function can receive an additional 90° phase shift for better mode-locking. The end mirror leads to a π phase shift and, thus, to a reproducible roundtrip solution of the wave equation, i.e., after a complete roundtrip, the pulse properties are reproduced.
Adding two $\lambda/2$-waveplates in the resonator, as shown in Fig. 2.5, extends the mode-locking parameter space which improves the laser handling and allows for the polarizer to be rotated back into the beam plane. Further, the fiber connected polarizer is replaced

Die approbierte gedruckte Originalversion dieser Diplomarbeit ist an der TU Wien Bibliothek verfügbar.
The approved original version of this thesis is available in print at TU Wien Bibliothek.
TU Bibliothek Your knowledge hub WIEN

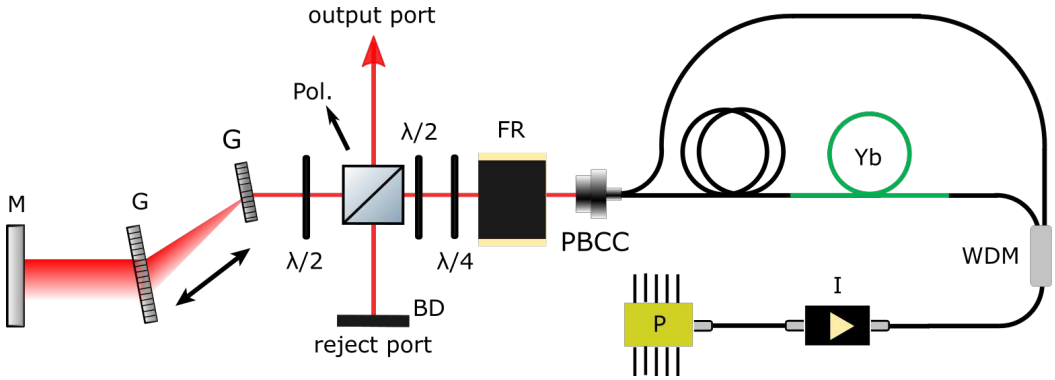

Figure 2.5: Schematic sketch of a realized figure-9 laser concept, where G is a grating, M is a mirror, Pol. is a polarization-dependent beam splitter, FR is a Faraday rotator, PBCC is a polarization beam combiner cube, $\lambda/2$ and $\lambda/4$ are the corresponding waveplates, P is the pump diode, I is the isolator, Yb is a Yb doped gain fiber, and WDM is a wavelength division mulitplexer.

by a polarization beam combiner with an integrated collimator (PBCC). The $\lambda/2$ and $\lambda/4$-waveplate pair between polarizer and NALM introduce the additional phase bias discussed above and also have influence on the wavelength selection (Sec. 2.3.2). The waveplate pair also controls the modulation depth of the NALM. The $\lambda/2$-waveplate next to the end mirror in combination with the grating compressor, the end mirror, and the out-coupling polarizer works as an intensity-dependent beam splitter.
Theoretically, with an ideal grating compressor without axis-specific phase shifts, the left most waveplate in Fig. 2.5 would need to be a $\lambda/4$-waveplate for complete polarization control. However, the grating compressor produces an axis-specific phase shift of 180° after a double pass, which requires that this $\lambda/4$-waveplate to be replaced by a $\lambda/2$-waveplate. This configuration guarantees a consistent roundtrip solution in the resonator with a defined intensity fraction of the laser beam passing the polarizer in the direction of the end mirror. The subsequent pass of the output coupler couples out the ratio of the pulse set by the $\lambda/2$-waveplate. In contrast, the other port works as a wavelength selector for the pulse formation, called reject port. The broadband gain spectrum of Yb allows different mode-locking states, which can be controlled by the combination of the $\lambda/2$ and $\lambda/4$-waveplates, the grating compressor, the end mirror alignment and the pump power. A detailed analysis of the angle of the waveplates depending on the phase shift, the modulation depth and a description of how this type of laser can be mode-locked can be found in [24].

2.3.1 Dispersion and self-phase modulation

Stable pulse operation requires the reproduction of the pulses after a complete cavity roundtrip. As mentioned above, the desired nonlinear effects in the NALM also have a strong influence on the spectral pulse shape. Besides this nonlinear effect, chromatic

Die approbierte gedruckte Originalversion dieser Diplomarbeit ist an der TU Wien Bibliothek verfügbar.
The approved original version of this thesis is available in print at TU Wien Bibliothek.
TU Bibliothek Your knowledge hub WIEN

dispersion has a strong influence on the temporal pulse shape. Furthermore, the gain saturation and Raman scattering also influence the time and frequency pulse shape. The most important contributions are the pulse broadening by SPM and dispersion of the laser components. To quantify the dispersion, the wavenumber k is expanded around a reference frequency ω_0, i.e.

$$k(\omega) = k_0 + \left.\frac{\partial k(\omega)}{\partial \omega}\right|_{\omega_0} (\omega - \omega_0) + \frac{1}{2} \left.\frac{\partial^2 k(\omega)}{\partial \omega^2}\right|_{\omega_0} (\omega - \omega_0)^2 + \frac{1}{6} \left.\frac{\partial^3 k(\omega)}{\partial \omega^3}\right|_{\omega_0} (\omega - \omega_0)^3 + \dots \tag{2.5}$$

The first contribution $k_0 = k(\omega_0)$ leads to a common phase shift, while the coefficient of the second term,

$$k^{'} \equiv \frac{\partial k}{\partial \omega} = \frac{1}{v_\mathrm{G}} \tag{2.6}$$

describes the time delay per unit length, which is the inverse group velocity v_G. The quadratic term in Eq. (2.5) contains the second order dispersion or group delay dispersion per unit length, which is

$$GVD = \frac{GDD}{L} := k^{''} \equiv \frac{\partial k^2}{\partial \omega^2} = \frac{\partial}{\partial \omega}\left(\frac{1}{v_\mathrm{G}}\right), \tag{2.7}$$

where L is the resonator length, and results in temporal pulse broadening or compression. The term

$$k^{'''} \equiv \frac{\partial k^3}{\partial \omega^3} \tag{2.8}$$

is defined as third order dispersion (TOD).
The GDD is now considered in detail because it is associated to a rapid change in the laser dynamics. It depends on the group velocity and is related to the refractive index, as

$$v_\mathrm{G} = \left(\frac{\partial k}{\partial \omega}\right)^{-1} = \left(\frac{\partial}{\partial \omega}\omega\, n(\omega)\right)^{-1} = \frac{c}{n(\omega) + \omega \frac{\partial n}{\partial \omega}} = \frac{c}{n_\mathrm{G}} \tag{2.9}$$

$$GDD = k^{''} L = \frac{n(\omega) + \omega \frac{\partial n}{\partial \omega}}{c} L \tag{2.10}$$

where $n(\omega)$ is the refractive index and n_G is the group refractive index. To calculate the group velocity in an optical fiber, the refractive index n must be replaced by the effective refractive index n_eff, which is defined by

$$\beta = n_\mathrm{eff} \frac{2\pi}{\lambda} = n_\mathrm{eff} k_\mathrm{Vac}. \tag{2.11}$$

Die approbierte gedruckte Originalversion dieser Diplomarbeit ist an der TU Wien Bibliothek verfügbar.
The approved original version of this thesis is available in print at TU Wien Bibliothek.
TU Bibliothek Your knowledge hub WIEN

Here, k_{Vac} is the vacuum wave number and β is defined by the propagation constant γ, which describes the phase change per unit length in the propagation direction,

$$A(z) = A(0)\exp(\gamma z), \tag{2.12}$$

where $A(z)$ is the complex amplitude of the light field and in lossless wave guides γ is a imaginary number, which leads to

$$\gamma = i\beta. \tag{2.13}$$

To calculate the refractive index of optically visible material, the Sellmeier equation [26] is an accurate method, which is valid as long as the absorption is negligible. The Sellmeier coefficients of the commonly used materials are tabulated (e.g. Ref. [27]). The GDD calculation of an optical fiber is complicated because the GDD consists of the material dispersion and the waveguide dispersion. Therefore the manufacturer's data are used to calculate the GDD of the fiber section of the laser. In the Yb gain region, the standard fiber has normal dispersion, and therefore an additional GDD compensation device has to be used. A grating compressor does this in a double-pass configuration. The GDD of the grating compressor is given by

$$GDD_{\mathrm{grating}} = -\frac{\lambda^3 L}{\pi c^2 d^2}\left[1 - \left(\frac{\lambda}{d} - \sin\vartheta_0\right)^2\right]^{-\frac{3}{2}}, \tag{2.14}$$

where L the gratings distance, c the speed of light, λ the wavelength, ϑ_0 the angle of incidence, $d = 1/g$ and g is the grooves density. The following paragraph discusses how the nonlinear effects influence the temporal and spectral shape of the pulse. The transfer function defines the intensity required to mode-lock the laser. In figure-9 lasers as discussed above, this threshold intensity can be reduced using the additional phase bias device to reduce the necessary phase shift. Even then, one must take into account the nonlinear effects on the temporal and spectral pulse shape. The high intensities lead to a self-phase modulation due to the Kerr effect. In the time domain, the Kerr effect introduces an additional intensity-dependent refractive index, defined by

$$\Delta n = n_2 I, \tag{2.15}$$

where I is the intensity of the electromagnetic wave and n_2 is the nonlinear refractive index, which is related to the third-order susceptibility $\chi^{(3)}$ as

$$n_2 = \frac{3}{4\epsilon_0 c\, n_0^2}\,\mathrm{Re}\left(\chi^{(3)}\right), \tag{2.16}$$

n_0 being the linear refractive index, c the speed of light and ϵ_0 the vacuum permittivity. The definition of nonlinear susceptibilities is based on a Taylor expansion of the polarization of the material as a function of the electric field, which is

$$P(E) = P_0 + \chi^{(1)}E + (1/2)\chi^{(2)}E^2 + (1/6)\chi^{(3)}E^3 + \ldots \tag{2.17}$$

Die approbierte gedruckte Originalversion dieser Diplomarbeit ist an der TU Wien Bibliothek verfügbar.
The approved original version of this thesis is available in print at TU Wien Bibliothek.
TU Bibliothek Your knowledge hub WIEN

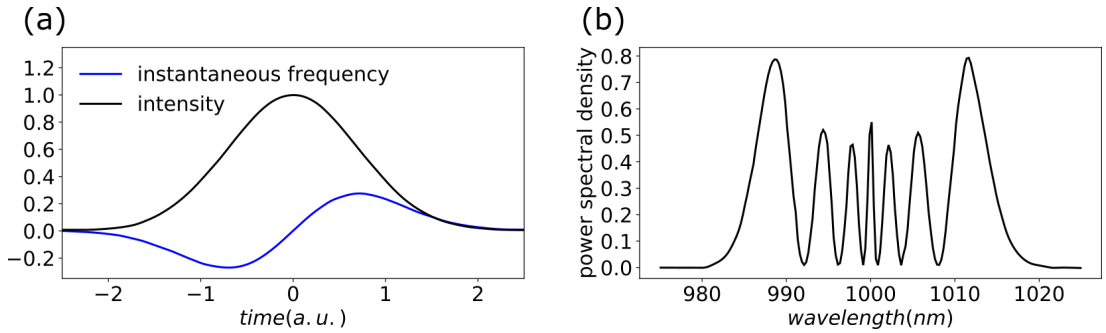

Figure 2.6: Effects of self-phase modulation (SPM). Temporal evolution of an unchirped pulse, which experiences SPM (a), and the oscillation of a power spectral density caused by too strong SPM which has destroyed the pulse (b).

Figure 2.6a shows a Gaussian pulse in the time domain and the instantaneous frequency introduced by SPM. This nonlinear chirp preserves the pulse duration when the influence of the Kerr effect occurs only in a short nonlinear material or is simultaneously reduced by other effects. The pulse is affected by the Kerr effect in the frequency domain, where spectrum modulation occurs. Too strong SPM can destabilize the pulse due to increasing oscillations, as illustrated in Fig. 2.6b. Therefore, a balanced system of SPM and GDD is the key to a working laser system, although the GDD chirp is linear, and that of the SPM is nonlinear. The indensity-independet behavior of the temporal broadening of the pulse introduced by the GDD compared to the temporal shortening of the pulse by the intensity-dependent Kerr effect leads to a small parameter space in which stable pulse formation is possible. The parameters corresponding to the GDD and SPM are determined by the wave equation of the laser system. An additional influence is the gain saturation, which can lead to a distortion of the pulse shape due to the decreasing gain. At a high repetition rate, the gain behavior approaches an average value. In the NALM, the counter-propagating pulses should ideally receive the same gain contribution.

2.3.2 Laser dynamics

To obtain a roundtrip solution of the resonator, the SPM, net-GDD, Raman scattering, and gain saturation have to cancel each other per roundtrip. The most straightforward nonlinear Schrödinger equation includes the Kerr effect and the GDD without further contributions. For this simplified equation, an analytical solution for the pulse propagation in a waveguide exists. The Hauser Master equation [28] is an extension of the Schrödinger equation and includes gain, attenuation, and a fast saturable absorber. An analytical solution also exists for this equation and leads to a soliton-like shaped pulse. The soliton solution is a chirp-free pulse that neither changes the temporal shape nor the spectral envelope over the entire cavity round trip. During soliton propagation, two side peaks, so-called Kelly sidebands, can occur in the spectrum which are a characteristic feature of a soliton. A periodical perturbation wave called dispersion wave generates these sidebands.

Die approbierte gedruckte Originalversion dieser Diplomarbeit ist an der TU Wien Bibliothek verfügbar.
The approved original version of this thesis is available in print at TU Wien Bibliothek.
TU Bibliothek Your knowledge hub WIEN

Besides the analytical soliton derived from the Hauser equation, a soliton-like solution exists, where the GDD increases the pulse duration during the cavity round trip. A grating compressor compresses the broadened temporal pulse to reach a stable solution. Such a pulse operation regime is called a stretched pulse regime. A dispersion wave also appears in this regime. In this regime, the Hauser Master equation has to be solved numerically. The net cavity group delay dispersion of such stretched solitons, which includes the GDD of the laser components and the dispersion behavior of the pulse dynamics, should be below zero. The smaller nonlinear chirp, which results from the lower intensity due to pulse breathing, offers the possibility to increase the average energy of the pulse.
The net-positive GDD regime works quite differently than the stretched soliton regime because the temporal pulse compression needs an additional pulse-shaping mechanism. An all-normal-dispersion laser (ANDi) is discussed in Ref. [28], where the pulse shaping happens in three steps. The first small pulse compression occurs through the strong self-phase modulation, which results in spectral pulse broadening and therefore temporal shortening. The second part of the pulse compression happens via the mode-coupling which forces the different chromatic path lengths are also into f_{rep} spacing. These lead to more frequency lines in the envelope and, therefore, to a pulse shortening. Finally, spectral filtering reshapes the pulse to a roundtrip solution.
The spectral filtering in the NALM laser can occur via chromatic dispersion. The chromatic dispersion temporally separates the different frequencies of the pulse. Due to the temporal envelope of the pulse, different frequencies correspond to different intensities and, therefore, different transfer functions. Additional filtering partially occurs due to the combination of the $\lambda/4$-waveplate, $\lambda/2$-waveplate, and the polarizer. These unwanted frequency components are eliminated at the reject port. The waveplate combination also controls the modulation depth of the NALM by introducing an unequal splitting ratio. The combination of different pump powers and waveplate positions results in a variety of solutions. The propagation dynamics of these different solutions are difficult to simulate because small changes of the parameters could significantly affect the pulse solutions. For a complete characterization of the output pulse that represents the intracavity solution, values of laser-specific variables are required, which are sketched in Fig. 2.7. These variables comprise:

- The repetition rate f_{rep} of a pulse train is defined by the reciprocal round trip time T_{R} when only a single pulse is running in the cavity.
- The pulse duration τ is defined as the FWHM of optical power plotted over time. The TBP gives the minimum pulse duration.
- The pulse energy E is the average power divided by the repetition rate. This holds only if there is no background wave. A well-known example for a background wave is a dispersion wave.

Die approbierte gedruckte Originalversion dieser Diplomarbeit ist an der TU Wien Bibliothek verfügbar.
The approved original version of this thesis is available in print at TU Wien Bibliothek.
TU Bibliothek Your knowledge hub WIEN

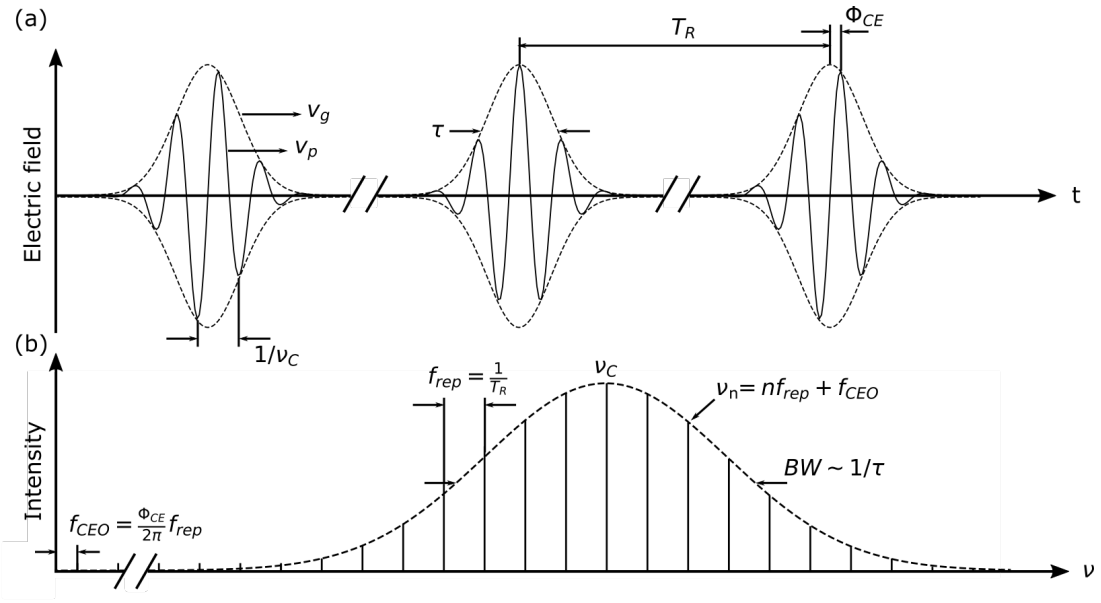

Figure 2.7: Schematic sketches of various variables in the time (a) and frequency (b) domain: phase velocity v_{p}, group velocity v_{G}, pulse duration at FWHM τ, pulse periode T_{R}, the carrier-envelope phase ϕ_{CE}, repetition rate f_{rep}, center frequency ν_{C}, the n^{th} frequency ν_{n}, the carrier-envelope offset frequency f_{CEO}, and the bandwith at FWHM (BW).

Die approbierte gedruckte Originalversion dieser Diplomarbeit ist an der TU Wien Bibliothek verfügbar.
The approved original version of this thesis is available in print at TU Wien Bibliothek.
TU Bibliothek Your knowledge hub WIEN

- The optical peak power defined as

$$P_\mathrm{p} = C_\mathrm{p} \frac{E_\mathrm{p}}{\tau_\mathrm{p}}, \tag{2.18}$$

  where C_p is a constant and depends on the pulse-shape. C_p takes the value 0.88 for a soliton-shaped pulse and 0.94 for a Gaussian-shaped pulse [29]. The peak power is necessary for the complete characterization because the peak power has a strong influence on nonlinear effects.

- The center frequency ν_center is defined as the spectral centroid (intensity-weighted mean of all frequencies). The center frequency is required for the net-GDD calculation.

- The carrier-envelope offset frequency f_CEO is defined as the phase delay between the carrier (electric field) of the light pulse and their envelope. In material, the group velocity is slightly smaller than the phase velocity, resulting in the carrier-envelope phase (CEP) relation.

- The chirp of a pulse describes the change in frequency of the electric field. The interaction of the material with the electric field leads to a change in the instantaneous frequency, which is described in detail in Sec. 2.3.1.

- The interesting noise properties are timing jitter (f_CEO phase noise), relative intensity noise (RIN), and phase noise of f_rep. The timing jitter states the deviation from the periodic pulse train formation, whereas the RIN shows the amplitude noise. The f_CEO noise couples to the pump noise, which is important for laser stabilization.

The characterization of optical pulses only makes sense, if a single pulse is running in the cavity which is called clean mode-locking. Clean mode-locking has to be verified by different approaches because different devices are only sensitive to multi-pulsing on different time scales.
The radio frequency (RF) analyzer is used to exclude double pulsing. Let us consider a second pulse within the laser cavity. If the time delay between the pulses is $T_\mathrm{R}/2$ (where T_R is the cavity roundtrip time), an additional fundamental frequency with $f = 1/(T_\mathrm{R}/2) = 2f_\mathrm{rep}$ is generated, see Fig. 2.8. The generation of the additional fundamental frequency generates a modulation on the radio frequency trace. However, if the separation is not $T_\mathrm{R}/2$ side peaks, wings on the signal occur, which indicate parasitic pulses. The minimum time between two pulses that can still be resolved is limited by the bandwidth of the photodiode in combination with the bandwidth for the radio frequency analyzer.
The optical spectrum analyzer (OSA) also gives an indication when double pulses occur in close proximity. The constant phase relations of the two pulses result in constructive and destructive interference of the common frequency components of the two pulses. Manifesting as an additional oscillation in the pulse spectrum. The detection of this oscillation is limited by the resolution of the OSA.

Die approbierte gedruckte Originalversion dieser Diplomarbeit ist an der TU Wien Bibliothek verfügbar.
The approved original version of this thesis is available in print at TU Wien Bibliothek.
TU Bibliothek Your knowledge hub WIEN

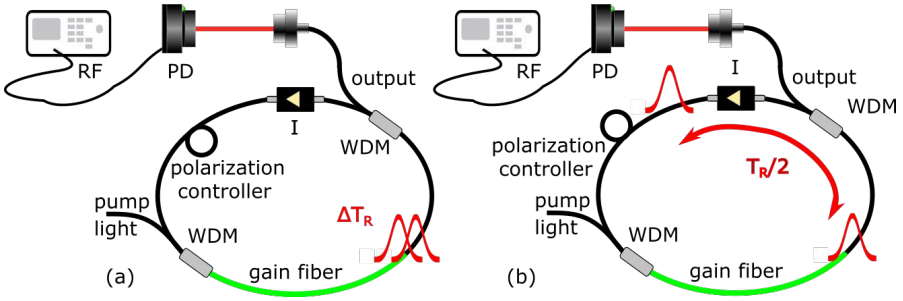

Figure 2.8: Schematic sketch of different variations of double pulsing inside a ring resonator. For small temporal pulse separations (a), the double pulse detection is limited by the bandwidth of the photodiode in combination with the bandwidth of the Oszillsocope or Radiofrequency analyzer used for detection. For large pulse separations (b), an envelope modulation of the higher harmonics of the repetition-rate will occur. Where RF stand for a radio frequency analyzer, PD a photo diode, I an isolator and WDM for wavelength division multiplexer.

In the presented study the exclusion of double pulses is is ensured via the aformentioned methods. However, further laser studies will allow for an improvement here through the measurement (by an $f - to - 2f$ interferometer) and analysis of the f_{CEO}, which is, however, out of scope of this work.

2.3.3 Net-GDD

While the pulse propagates through the resonator, a time-dependent pulse broadening occurs not only due to chromatic dispersion but also due to the propagation dynamics, discussed in Sec. 2.3.2. Therefore a net-GDD is introduced, which is composed of the so-called cold cavity GDD of the device components and the propagation dispersion. W.H. Knox [30] developed a measurement method for the net-GDD of a laser system. The concept is based on a spatial wavelength separation by refraction and subsequent wavelength selection of the light beam inside the laser cavity. The grating compressor implemented in the laser design already generates such a frequency-dependent spatial dispersion and is, therefore, a suitable position to place a moving slit for spectral selection (see Fig. 2.9). This measurement is only useful for fiber lasers with a broadband gain source since a tunable center wavelength is necessary for the analysis. Important properties are

$$T_{\mathrm{roundtrip}}(\omega) = \frac{1}{f_{\mathrm{rep}}(\omega)} \tag{2.19}$$

and

$$\frac{\partial k(\omega)}{\partial \omega} = \frac{T_{\mathrm{roundtrip}}(\omega)}{L_{\mathrm{cavity}}}, \tag{2.20}$$

Die approbierte gedruckte Originalversion dieser Diplomarbeit ist an der TU Wien Bibliothek verfügbar.
The approved original version of this thesis is available in print at TU Wien Bibliothek.
TU Bibliothek Your knowledge hub WIEN

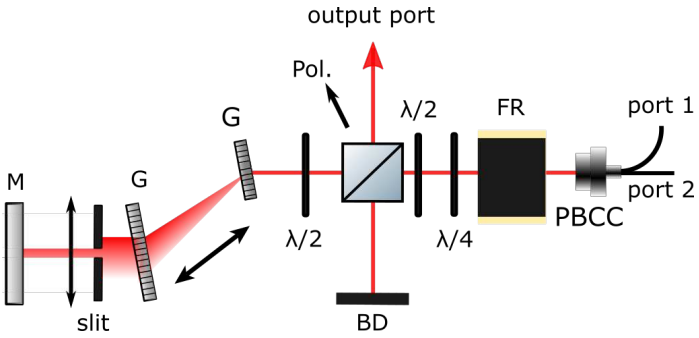

Figure 2.9: Schematic sketch of a Knox-measurement setup, where slit is racer blade gape mounted on a micrometer stage, FR is a Faraday rotator, G is a grating, Pol. is a polarizer, PBCC is a polarization beam combiner cube, M is a mirror, and $\lambda/2$ and $\lambda/4$ are the corresponding waveplates.

where L_{cavity} is the cavity length. Using Eqs. (2.19) and (2.20) as inputs to Eq. (2.7) one obtains

$$GDD = \frac{\partial}{\partial\omega}\left(\frac{T_{\text{roundtrip}}(\omega)}{L_{\text{cavity}}}\right) L_{\text{cavity}} = \frac{T_{\text{roundtrip}}(\omega)}{\partial\omega} = \frac{\partial}{\partial\omega}\left(\frac{1}{f_{\text{rep}}(\omega)}\right). \tag{2.21}$$

Here, $f_{\text{rep}}(\omega)$ is also called the group delay and is measured with the help of the RF analyzer and OSA. A slit is shifted through the laser beam and the resulting changes in f_{rep} are measured with the RF analyzer, whilst the changes in the optical spectrum are recorded using the OSA. The central wavelength is determined as the centroid of the area of the optical spectrum. The value of f_{rep} is obtained from averaging several independent measurements.
Assuming that higher than third-order dispersion can be neglected, a quadratic fit through the data gives a smooth function $f_{\text{rep}}(\omega)$. The net-GDD can than be simply obtained from the derivation of the analytic function.

2.3.4 Laser components

In this section, we discuss the most important laser components that are used in the presented studies.

Polarization maintaining fiber. A polarization maintaining fiber consists of a fiber core, two stress elements and cladding. Linearly polarized light can propagete in such a fiber while maintaining its polarization if it is properly coupled into the fiber. The unavoidable birefringence of optical fibers is exploited in polarization maintaining fibers by introducing two stress elements that artificially increase the internal birefringence. This causes the two polarization modes to propagate with different phase velocities making it impossible for the two modes to couple to each other.

Die approbierte gedruckte Originalversion dieser Diplomarbeit ist an der TU Wien Bibliothek verfügbar.
The approved original version of this thesis is available in print at TU Wien Bibliothek.
TU Bibliothek Your knowledge hub WIEN

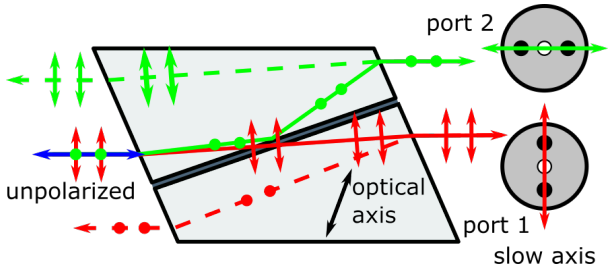

Figure 2.10: Schematic sketch of the working principal of the Wollaston polarization beam splitter in the PBCC.

X-coupler and wavelength-division-multiplexer (WDM). An X-coupler and WDM operate on the same principle: two fibers are brought so close together that the the guided light fields start to interact, called evanescent field. The interation happens because the propagating pulse extends transversally not only in the fiber core but also in the core-cladding. The X-coupler ratio can be controlled by twisting and stretching the two fibers during manufacturing. The result of the interaction depends on the length of the twisted part of the fibers since the intensity between the two fibers changes periodically. For example, an X-coupler with a 50:50 splitting ratio splits each input into equal output powers.
The WDM has the same design as an X-coupler, but one port is not used and is therefore blocked within the WDM. Due to the chromatic dispersion of the used fiber, different wavelengths have different path lengths, which is exploited in the manufacturing process. This wavelength-dependent construction leads to a non-reversible propagation of a specific wavelength.

Polarization Beam Combiner Cube (PBCC). The PBCC, shown in Fig. 2.10, is a customized item that splits the beam depending on its polarization, using a Wollaston prism, and separately couples them to the two slow axes of the polarization-maintaining fibers at the output. It is worth mentioning that the two fibers are tilted by 90° against each other. A collimator at the free-space port completes the customized device.

Grating compressor. The grating compressor uses diffraction to separate the different wavelengths spatially, resulting in different optical path lengths, which leads to a phase delay for longer wavelengths. The grating compressor only compensates second-order dispersion (GDD), and therefore higher-order dispersion has to be managed by the laser design. The calculation of the GDD is described in more detail in Sec. 2.3.1 and given by equation (2.14).
An additional behavior of the grating compressor was found during the alignment process observing that the $\lambda/4$ waveplate in double pass did not result in a full switching ratio at the polarizer in Fig. 2.5. By exchanging, the $\lambda/4$ by a $\lambda/2$-waveplate full switching at the polarizer is possible, rom which it follows that the grating compressor behaves lake a $\lambda/2$ plate upon double pass.

Die approbierte gedruckte Originalversion dieser Diplomarbeit ist an der TU Wien Bibliothek verfügbar.
The approved original version of this thesis is available in print at TU Wien Bibliothek.
TU Bibliothek Your knowledge hub WIEN

Faraday rotator. The FR tilts the electrical field via the influence of a magnetic field on a transparent medium, independently of the propagation direction. The magnetic flux density B direction is equal or opposite to the propagation direction and the rotation angle is given by

$$\alpha_{\mathrm{FR}} = V \cdot B \cdot L, \tag{2.22}$$

where V is the Verdet constant of the material and L the length of the transparent medium. Using the FR in the double pass, the rotations add up instead of canceling each other, like in waveplates.

Die approbierte gedruckte Originalversion dieser Diplomarbeit ist an der TU Wien Bibliothek verfügbar.
The approved original version of this thesis is available in print at TU Wien Bibliothek.
TU Bibliothek Your knowledge hub WIEN

3 Experimental Setup and Methods

The components of the following laser setup are all commercially available and a detailed list of the components is found in chapter 6 in Tab. 6.1. However, as we noted significant variation in their performance, we designed different tests to investigate actual performance. The measurement instruments used are listed in chapter 6 in Tab. 6.2.
The first setup is designed to test the pump laser diode in combination with the PM-isolator, see Fig. 3.1(a). We spliced polarization-maintaining fibers with an Ericsson FSU 995 PM fiber splicer. This splicer is capable of splicing PM fibers by controlling the orientation of their stress elements. We measured the laser slope of the pump diode with a thermal power meter, see Fig. 3.1(b). The measured laser slope shows excellent agreement with the data provided by the manufacturer. Measuring the spectrum of the pump-diode for different output powers over the whole pump current range proves the stability of the pump-diode, see Fig. 3.1(c). For pump currents up to 200 mA, the spectrum changed its shape and shifts 0.5 nm towards higher wavelengths. Both spectral shape and center wavelength do not change above 200 mA. The temperature is stable from 21 °C to 28 °C (Fig. 3.1(d)). When compared to Fig. 2.1 its obvious that the pump spectrum overlaps entirely with the maximum range of the Yb absorption-cross-section.
Another critical component of the laser setup is the polarization beam combiner cube (PBCC). The PBCC is the only custom-made part, schematically sketched in Fig. 2.10. The Wollaston polarization beam splitter separates an incoming beam into an s-, and a p-polarized beam and couples both beams into the slow axis of each of the two PM single-mode fibers. To couple each polarization into the slow axis of the fiber, the fibers are tilted against each other by 90°. An intensity-dependent camera measures distortion and divergence over different distances from 10 cm to 90 cm of the beam profile, the test setup is shown in Fig. 3.2(a). It should be noted that it is important to guide the correct beam into the camera, as the Wollaston-prism produces two unwanted side reflections of low intensity in addition to the main beam (Fig. 2.10).
Yb, as the gain medium, enables broadband lasing at around 1000 nm to 1100 nm. To test operation over a wide bandwidth, we injected two test laser beams with central wavelengths of 1030 nm and 1036 nm into the different ports. The pulses that were guided into the PBCC stemmed from another figure-9 laser, shown in Fig. 3.2(b). The free space part of the laser is 22 cm (44 cm in double pass). For this path length the divergence and distortion is of sufficient quality. Figure 3.2(c) shows the different beam profiles. After testing of the individual laser components, the laser setup was built, as shown in Fig. 3.3.
A micrometer stage controls the distance of the gratings, which manages the net-GDD of the laser system. Therefore, we mounted one of the gratings and the end mirror on a micrometer translation stage. The combined positioning of the end mirror and the grat-

Die approbierte gedruckte Originalversion dieser Diplomarbeit ist an der TU Wien Bibliothek verfügbar.
The approved original version of this thesis is available in print at TU Wien Bibliothek.
TU Bibliothek Your knowledge hub WIEN

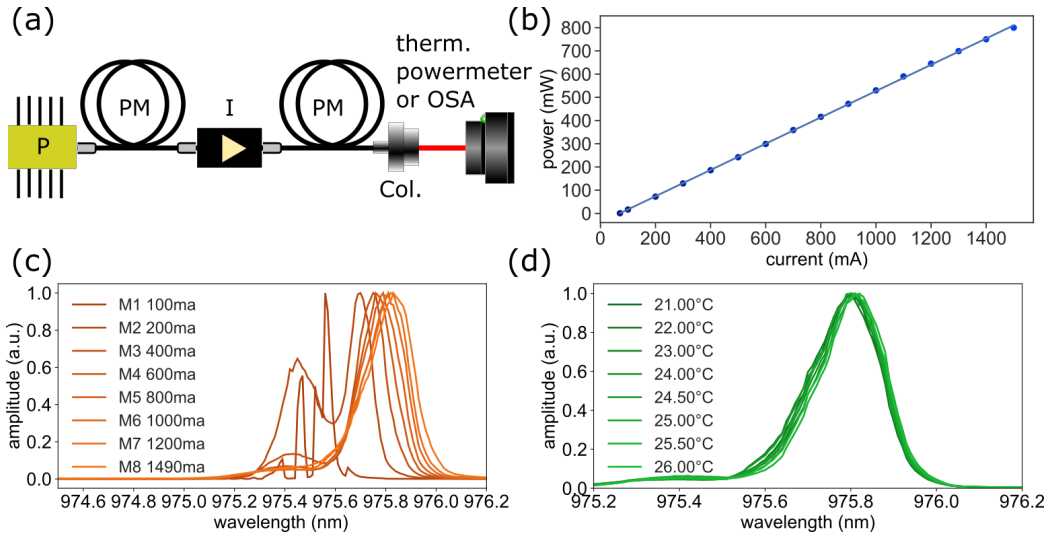

Figure 3.1: Schematic sketch of the setup which is used test the pump laser diode and to produce the performance graphs of key properties. The test setup of the pump diode in combination with the pm-isolator (a), the laser slope of the setup (b), spectra series by changing the pump current (c), and spectra series obtained various temperatures (d).

ing avoids misalignment of the cavity by changing the grating distance. The beam ray that is outgoing from the PBBC is guided through two pinholes for horizontal alignment. Next, we placed the polarizer, the micrometer stage with the grating compressor, and the end mirror in the laser setup. For a rough alignment, a detector viewer card (for the near-IR area (NIR)) makes the laser beam visible. A back reflection to the PBCC occurs by adjusting the end mirror mount. Implementing the waveplates gives a handle over the splitting ratio of the polarizer and, therefore, increases the amount of visible light. The precise alignment happens by maximizing the intensity displayed at the power meter connected to the second PBCC port. Therefore, all implemented waveplates adjusted such that the full response is on the second port, as shown in Fig. 3.4.
The cavity is closed by splicing the fiber ring without replacing the PBCC, to conserve the alignment. It is worth to mention that this alignment process is only possible if a laser source in the same wavelength region exists in the laboratory. However, since other crucial parts of the laser setup were already in place using an external laser source was no option. Therefore, another alignment procedure was used. In the used alignment procedure, the alignment light occurs from amplified spontaneous emission (ASE), which is less intense than the external laser source. It is to note that the used alignment procedure is slightly more complicated and carries the risk of damaging the gain fiber. For ASE alignment, the pumping power must be low, since a Q-switch can destroy the laser components.
Such a Q-switch occurs from pumping the amplification fiber without a closed or interrupted resonator, which results in high energy storage in the gain fiber. This energy

Die approbierte gedruckte Originalversion dieser Diplomarbeit ist an der TU Wien Bibliothek verfügbar.
The approved original version of this thesis is available in print at TU Wien Bibliothek.
TU Bibliothek Your knowledge hub WIEN

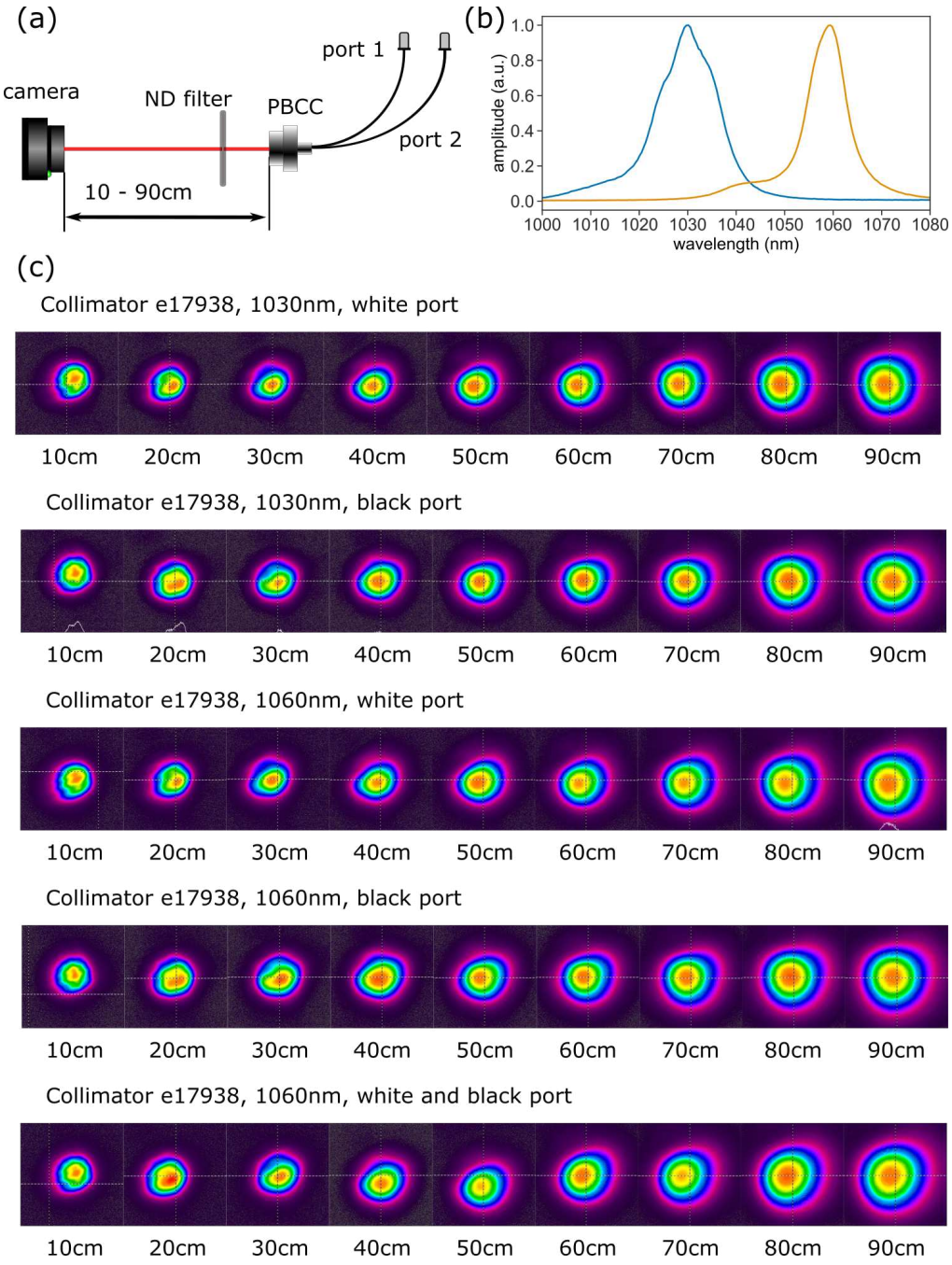

Figure 3.2: Schematic sketch of the test setup and beam profiles acquired for several distances from the outcoupler. Test setup for obtaining beam profiles, where PBCC is a polarization beam combiner cube, and ND-filter is a neutral density filter (a), the spectrum that is injected in the PBCC (b), and the recorded beam profiles (c).

Die approbierte gedruckte Originalversion dieser Diplomarbeit ist an der TU Wien Bibliothek verfügbar.
The approved original version of this thesis is available in print at TU Wien Bibliothek.
TU Bibliothek Your knowledge hub WIEN

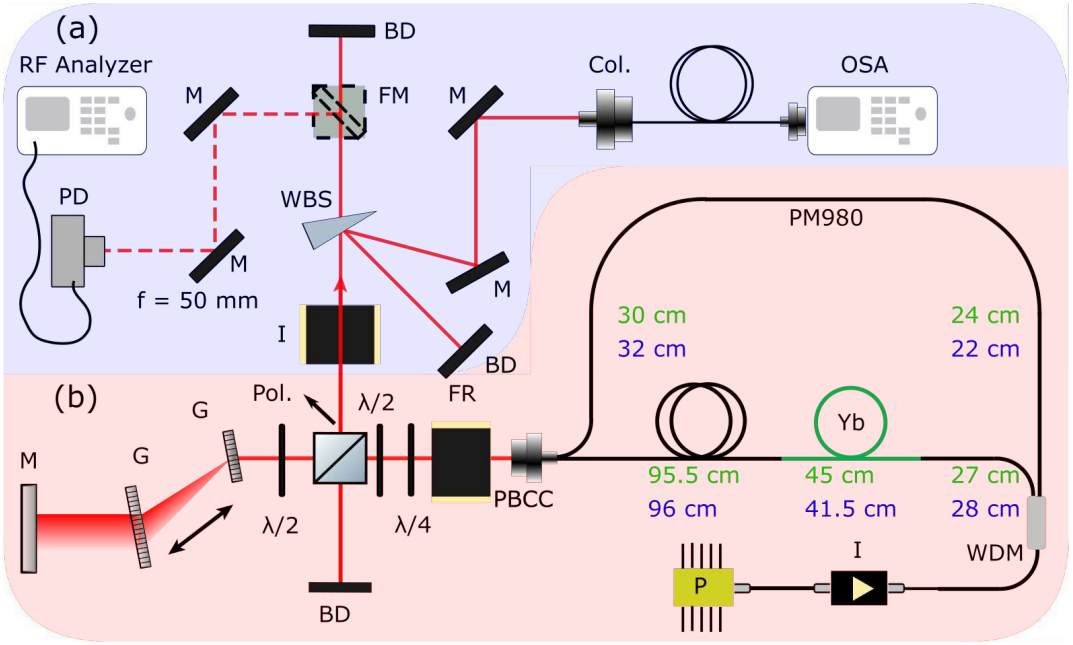

Figure 3.3: Schematic sketch of the laser setup including its diagnostic part. The diagnostic part is sketched in the blue area, where I is an isolator, WBS is a wedge, FM is a flip mirror, M is a mirror, BD is a beam dump, PD is a photo diode, Col. is a collimator (a). The laser setup is sketched in the pink area with the different fiber lengths for laser 1 and laser 2, where G is a grating, Pol. is a poalrization dependent beam splitter, FR is a Faraday rotator, PBCC is a polarization beam combiner cube, $\lambda/2$ and $\lambda/4$ are waveplates of respective thickness, P is the pump diode, Yb is a Yb doped gain fiber, and WDM is a wavelength division mulitplexer (b).

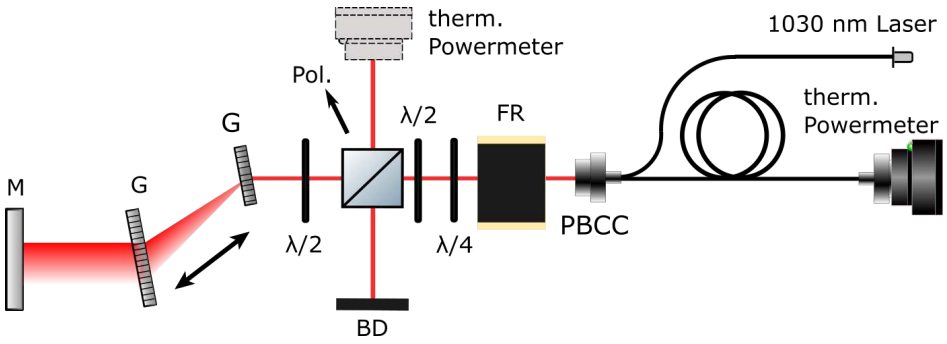

Figure 3.4: Schematic sketch of the freespace alignment setup, where FR is a Faraday rotator, G is a grating, Pol. is a polarizer, PBCC is a polarization beam combiner cube, M is a mirror $\lambda/2$ and $\lambda/4$ are waveplates, and P is the pump diode.

Die approbierte gedruckte Originalversion dieser Diplomarbeit ist an der TU Wien Bibliothek verfügbar.
The approved original version of this thesis is available in print at TU Wien Bibliothek.
TU Bibliothek Your knowledge hub WIEN

can be suddenly extracted by a Q-switch, which can lead to a pulse strong enough to damage the laser components.
The upper limit of the alignment pump current used during the alignment was around 150 mA, where no danger of damaging any of the components exists. During initial alignment, a reliable sign of beginning CW lasing is the observation of decreasing brightness of the gain fiber, observed with a "near-IR-viewer".
For precise alignment of the laser cavity, we first had to build up the diagnostic part, shown in Fig. 3.3. Before we discuss the diagnostic part in detail, it should be mentioned that the precise alignment of the laser requires a sensitive measuring instrument, like an OSA which can be used to monitor changes in the optical spectrum. A crucial parameter is the lasing threshold. The lasing threshold is defined as the minimum pump power required for the oscillator to start lasing. We reached the laser threshold by adjusting the two $\lambda/2$-waveplates, the $\lambda/4$-waveplate, and the position of the end mirror to provide maximum feedback into the cavity. The diagnostic part and the laser are separated by an isolator, which protects the seed laser from back reflections. After the isolator, a so-called "wedge" splits the laser beam into two laser paths. The reflected beam propagates through a $\lambda/2$-waveplate and a polarizer into the OSA. The $\lambda/2$-waveplate protects the OSA, which requires relatively low input power. The beam that is transmitted through the wedge and carries the major part of the output power, is guided to the photodiode. A coaxial cable connects the RF analyzer to the photodiode in which is illuminated by the laser beam via an additional collimator.

Die approbierte gedruckte Originalversion dieser Diplomarbeit ist an der TU Wien Bibliothek verfügbar.
The approved original version of this thesis is available in print at TU Wien Bibliothek.

4 Results

The characterization of the figure-9 laser presented in this work encompasses systematic exploration of the main parameter space. These are the orientation of the $\lambda/2$ and $\lambda/4$-waveplates, the relative distance of the gratings, and position and orientation of the end mirror. We scanned the full range of grating separations where clean mode-locking occured and present a selection of representative operation states. Therefore, we have analyzed all fundamental characteristics of the laser, limited by the measurement setup and the resolution of the instruments.
In this work I check for clean mode-locking in the following way: I monitor the intracavity spectrum using the OSA and verify that no additional modulation on the spectrum is present to exclude double pulsing. I measure the repetition rate and higher harmonics using an RF analyzer to check their envelope for periodic oscillations, which indicates unclean mode-locking.
The data that I have prepared and presented here are also summarized in the publication [24]. Based on this thesis the analysis of the mode-locking states was extended in the publication. Subsequent investigations on the existing laser setup also included the detection of the carrier envelop offest fequency via a $f-\mathrm{to}-2f$ measurement. The f_{CEO} detection further proved clean mode-locking for all the states presented here.
Furthermore, additional side peaks in the RF-trace indicate that parasitic pulses are generated in the cavity besides the main pulse. We have catalogued the clean mode-locking states found in this work in a net-GDD vs. wavelength map, which gives an overview of the different mode-locking regimes. The Knox-measurement can be used for the net-GDD measurements if the laser is stable enough such that a slit can be shifted in the beam without damaging the pulse lasing. In addition, we investigated the starting behavior of the different states by measuring their laser slopes.
In the course of the measurements, the laser system got damaged by a Q-switch caused by a misalignment during the adjustment of the laser. The investigation of the possible causes pointed to a damaged WDM, which we subsequently replaced. The rebuild slightly changed the fiber length ratios, resulting in a deviation of f_{rep}, the net-GDD, exact control parameters (grating separation, wave plate orientations, pump power, position of the end mirror) corresponding to clean mode-locking states compared to the first configuration (hereafter laser 1). Nevertheless, the new laser setup (hereafter laser 2) proves the reproducibility of the different laser states. Figure 4.1 shows the net-GDD map of the clean mode-locking states of laser 1 and laser 2. The labels "state 1–9" correspond to clean mode-locking states of laser 1; the corresponding net-GDD curves are solid lines. The remaining labels "state 10–15" correspond to laser 2 with dashed net-GDD lines. The difference in fiber length between the two lasers is 1.5 cm, which is less than 1% of the fiber length. The asymmetric placement of the gain fiber also differs

Die approbierte gedruckte Originalversion dieser Diplomarbeit ist an der TU Wien Bibliothek verfügbar.
The approved original version of this thesis is available in print at TU Wien Bibliothek.
TU Bibliothek Your knowledge hub WIEN

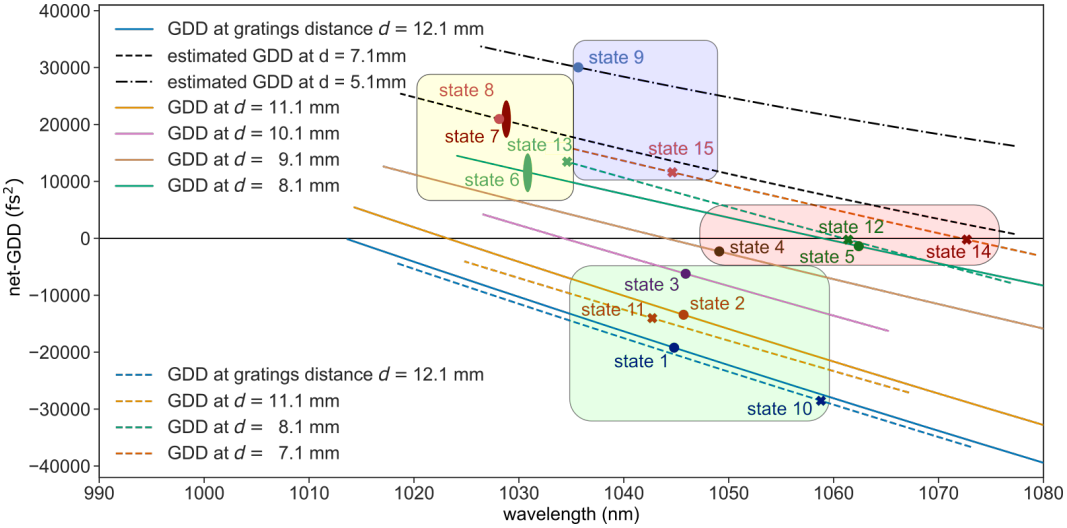

Figure 4.1: Net-GDD map of both lasers. Clean mode-locking states are marked by dots (for laser 1) and crosses (for laser 2). Lines indicate the corresponding GDD curves (solid for laser1, dashed for laser 2). The two black lines represent estimations with no adequate existing dataset.

in the two experimental setups, as shown in Fig. 3.3.
First, we discuss the clean mode-locking states with their characteristic behavior, and finally, the corresponding net-GDD slopes. We grouped the different clean mode-locking states into regimes according to their spectral shape. The regimes also depend on the net-GDD, which leads to the naming of the individual GDD regimes. There are the negative net-GDD regime, the near-zero net-GDD regime, the positive net-GDD regime, and the max positive net-GDD regime.

4.1 Characteristic regimes

4.1.1 Negative net-GDD regime

Figure 4.2 shows the optical spectra and corresponding repetition rates in a range of 700 MHz of the negative net-GDD regime. The states 1–3 are realized using almost the same waveplate angles,and exhibit almost the same pump power, output power, and an efficiency of up to 15%. The main distinguishing parameter is the distance of the gratings, which affects the spectra and the repetition rate. The FWHM of the spectra increased by reducing the grating separation. The center wavelength of the spectra changed only slightly. The change in the repetition rate results from the additional path length increase caused by the end mirror shift and an additional contribution of the grating compressor due to the greater frequency-dependent path lengths. This change in length is due to the joint mounting of the grating and end mirror. On the other hand, the differences of the center wavelength and the waveplate angle between state 10 and state 11 result

Die approbierte gedruckte Originalversion dieser Diplomarbeit ist an der TU Wien Bibliothek verfügbar.
The approved original version of this thesis is available in print at TU Wien Bibliothek.
TU Bibliothek Your knowledge hub WIEN

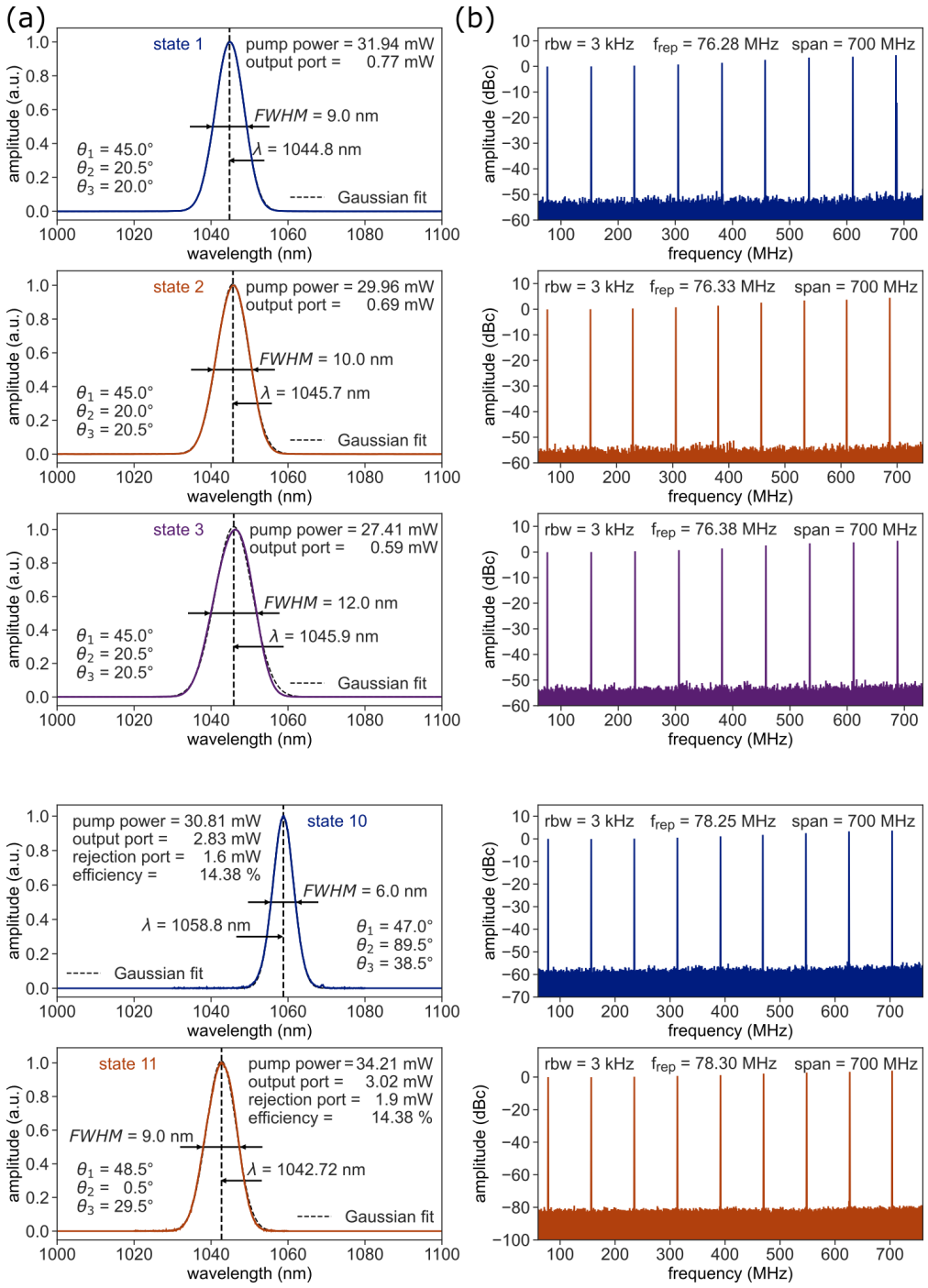

Figure 4.2: Optical spectra and repetition rates. Spectral shapes of the negative net-GDD regime fitted with a Gaussian and $sech^2$ function, where the FWHM, the centroid wavelength of the area under the spectrum, and characteristic powers are marked and the θ_i's are the corresponding waveplate angles (a). The recorded f_{rep} with a span of 700 MHz and a resolution-bandwidth of 3 kHz (b).

Die approbierte gedruckte Originalversion dieser Diplomarbeit ist an der TU Wien Bibliothek verfügbar.
The approved original version of this thesis is available in print at TU Wien Bibliothek.
TU Bibliothek Your knowledge hub WIEN

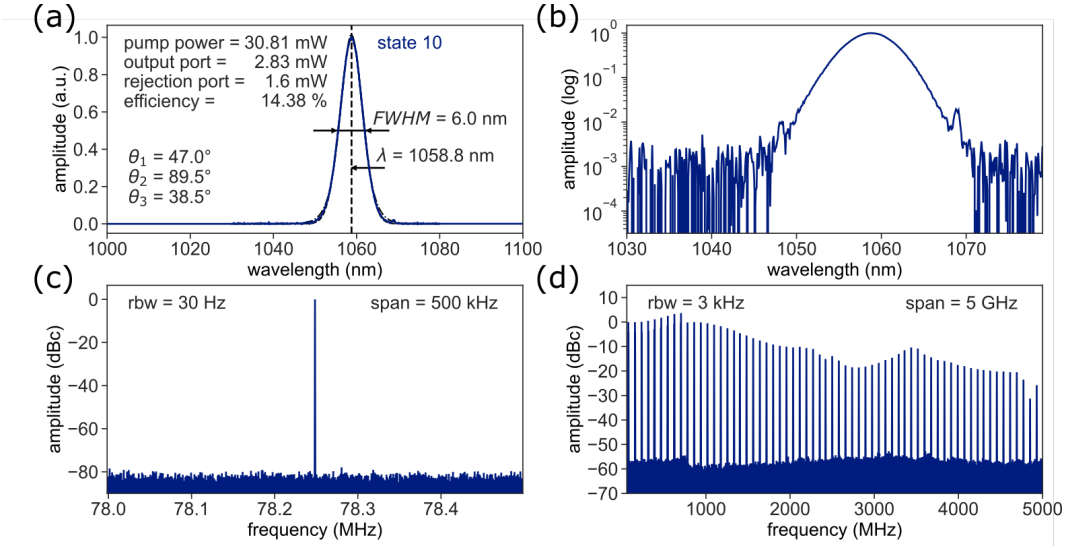

Figure 4.3: Characterization that is used to examine a clean mode-locking state. The optical spectrum with a Gaussian fit to the measured data and laser setup data (a), the spectrum in log scale (b), the first f_{rep} with a span of 500 kHz (c) and f_{rep} trace with a span of 5 GHz (d).

from the laser threshold alignment. We optimized CW threshold alignment for each grating distance for the characterization of laser 2. The large differences in the center wavelength result from unsufficient positioning accuracy of the end mirror, because the screw threads are too rough for alignment.

We discuss clean mode-locking based on state 10, representative for all states. Figure 4.3a and b show the optical spectrum in linear and logarithmic scale. The spectral shapes show no signs of oscillation and, therefore, no double pulsing, as discussed in Sec. 2.3.2. The repetition rate in a span of 500 kHz and 5 GHz is shown in Fig. 4.3c and d. The RF trace with a span of 5 GHz (Fig. 4.3d) indicates a slight variation of the f_{rep} envelope, which was caused by the freqency-depented photodiode. The repetition rate measured at a span of 500 kHz (Fig. 4.3c) and a resolution-band-with of 30 Hz excludes a parasitic pulse down to a temporal resolution of less than 0.2 ns. The spectrum of state 10 has a Gaussian shape (Fig. 4.3a) which indicates a stretched pulse behavior, as discussed in Sec. 2.3.2. The weak deviation from the stretched-soliton solution, which is determined from the Hauser-Master equation (based on a slow saturable absorber), results from the use of a fast saturable absorber (NALM) and additional filtering behavior of the actual laser setup. Besides, the spectrum (Fig. 4.3b) shows Kelly sidebands, which appear more clearly on the logarithmic scale. The Kelly sidebands indicate a dispersion wave running in the background. The excess energy of the pulse solution is transferred to the dispersion wave and therefore has the same periodicity. The transferred energy further reduces the output power of the laser. The similar properties of the negative net-GDD states compared to the stretched soliton solution lead to the term "Gaussian stretched

Die approbierte gedruckte Originalversion dieser Diplomarbeit ist an der TU Wien Bibliothek verfügbar.
The approved original version of this thesis is available in print at TU Wien Bibliothek.
TU Bibliothek Your knowledge hub WIEN

pulse solution."

4.1.2 Near-zero net-GDD regime

The negative net-GDD states merge into the near-zero net-GDD regime, see Fig. 4.4. State 4 represents the transition from the Gaussian-shaped stretched pulse into the typical shape for near-zero net-GDD, which has an additional growing lateral peak. The waveplate angles are still the same as in states 1–3 but the grating separation has been further reduced. A slight shift of the center wavelength to higher wavelengths and an additional deformation of Gaussian shape is visible. The mode coupling at 8.1 mm grating separation requires different waveplate angles and higher pump power. The clean mode-locking states 5 and 12 generate an output power of up to 4 mW yielding an efficiency of up to 30%. Clean mode-locking in the near-zero net-GDD regime at 7.1 mm grating separation requires an adjustment of the end mirror with respect to the other states. We manipulate the end mirror in such a way that the spectrum shifts to a higher wavelength.

4.1.3 Positive net-GDD regime

The next regime under discussion is the positive net-GDD regime. The spectral shapes and repetition rates of the respective states 6–8 and 13 are shown in Fig. 4.5. It consists of two different output powers, the main difference being the angle of the first $\lambda/2$-waveplate (θ_1). State 6 and state 13 show almost the same spectrum, pump power, output power, and an efficiency of more than 50%. State 7 starts mode-locking at the upper limit of the pump diode current and shows, therefore, the highest output power. Laser 1 is measured without recording the values for the reject port and therefore there are no efficiency values for these states. State 8 with its high pump power and low output power, suggests that a large part of the power coupled out at the reject port.

4.1.4 Max positive net-GDD regime

The last collection of spectra is called the "max positive net-GDD regime." A small and sharply peaked spectrum is characteristic for this regime, see Fig. 4.6. The FHWM is typically 1 nm, which should not be confused with a CW breakthrough. During the stability tests of laser 1, a Q-switch damaged the WDM and prevented the complete recording of the dataset.

4.2 Laser slopes

After discussing the spectra of the different net-GDD regimes, we investigate the mode-locking behavior using the laser slopes. A characteristic laser slope exists for the negative, positive, and max-positive net-GDD regime, shown in the top, middle and bottom panel of Fig. 4.7 respectively. The laser slope of the Gaussian stretched pulses shows that a lot of over-pumping is necessary to achieve mode-locking. A step in the slope indicates the

Die approbierte gedruckte Originalversion dieser Diplomarbeit ist an der TU Wien Bibliothek verfügbar.
The approved original version of this thesis is available in print at TU Wien Bibliothek.
TU Bibliothek Your knowledge hub WIEN

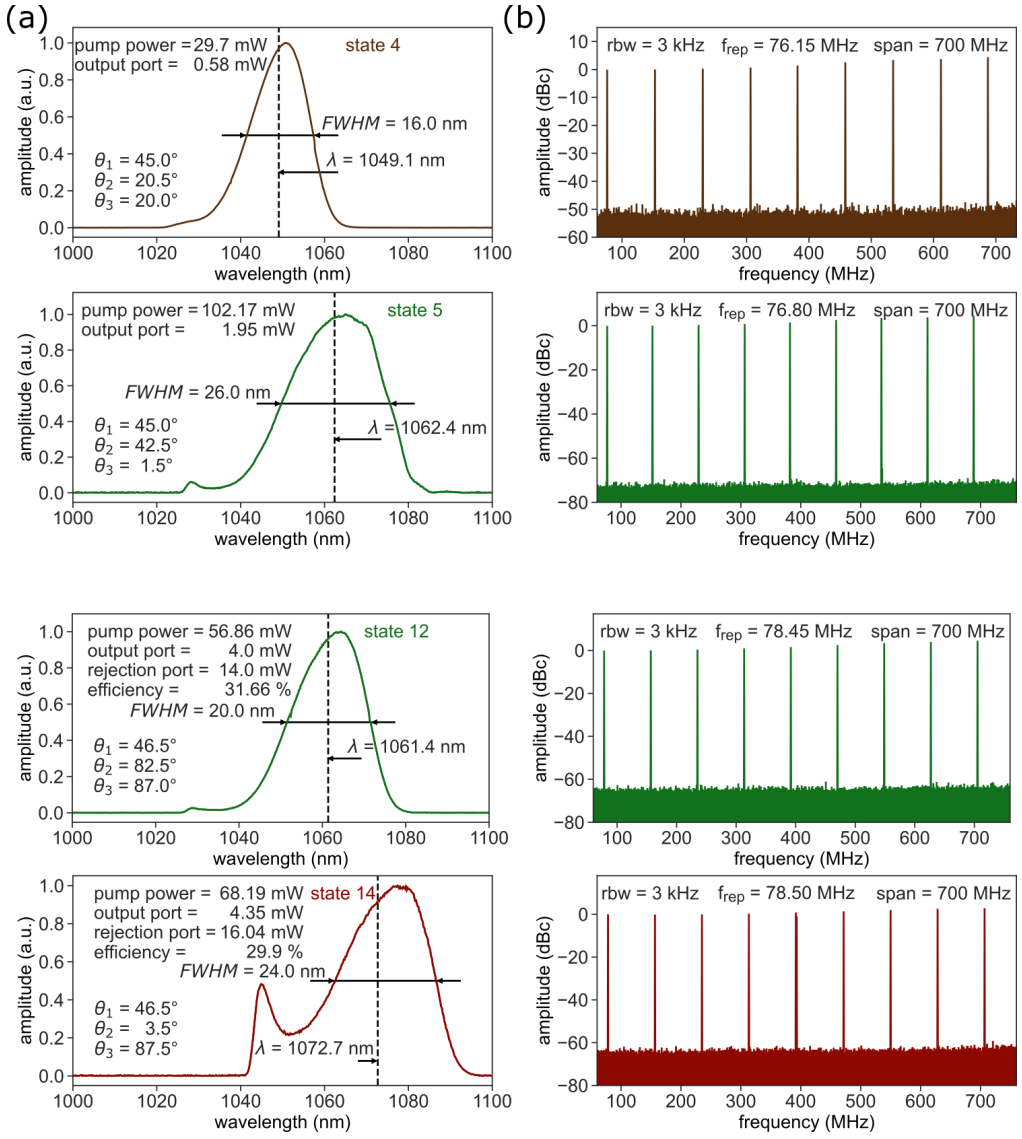

Figure 4.4: Optical spectra and repetition rates. Spectral shapes of the near-zero net-GDD regime with the FWHM, the centroid wavelength and characteristic powers, where the θ_i's are the corresponding waveplate angles (a). The f_{rep} recorded with a span of 700 MHz and a resolution-bandwidth of 3 kHz (b).

Die approbierte gedruckte Originalversion dieser Diplomarbeit ist an der TU Wien Bibliothek verfügbar.
The approved original version of this thesis is available in print at TU Wien Bibliothek.
TU Bibliothek Your knowledge hub WIEN

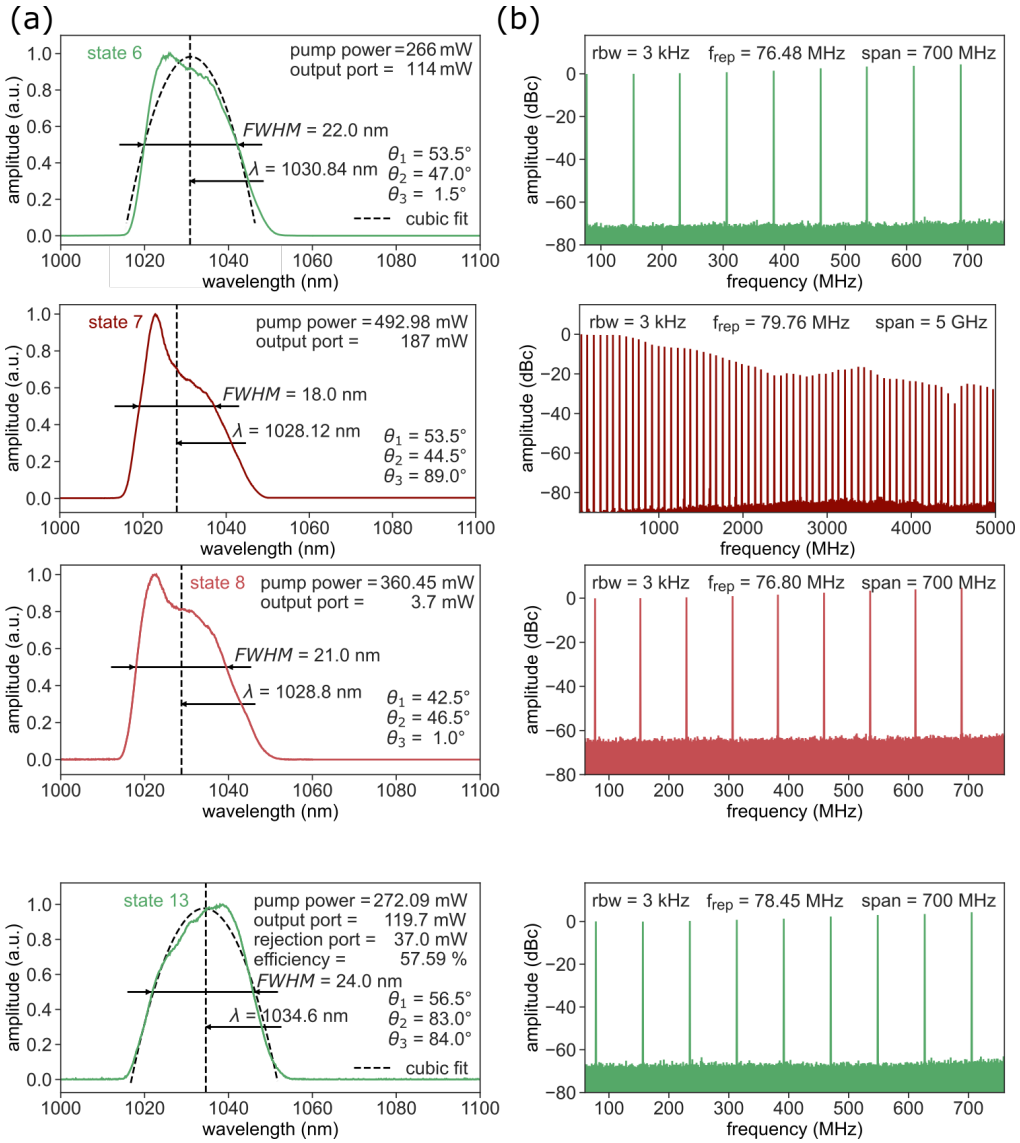

Figure 4.5: Optical spectra and repetition rates. Spectral shapes of the positive net-GDD regime with a parabolic fit, the FWHM, the centroid wavelength, and characteristic powers, where the θ_i's are the corresponding waveplate angles. The f_{rep} recorded with a span of 700 MHz and a resolution-bandwidth of 3 kHz (b). State 7 shows a span of 5 GHz since the laser was damaged during the measurements.

Die approbierte gedruckte Originalversion dieser Diplomarbeit ist an der TU Wien Bibliothek verfügbar.
The approved original version of this thesis is available in print at TU Wien Bibliothek.
TU Bibliothek Your knowledge hub WIEN

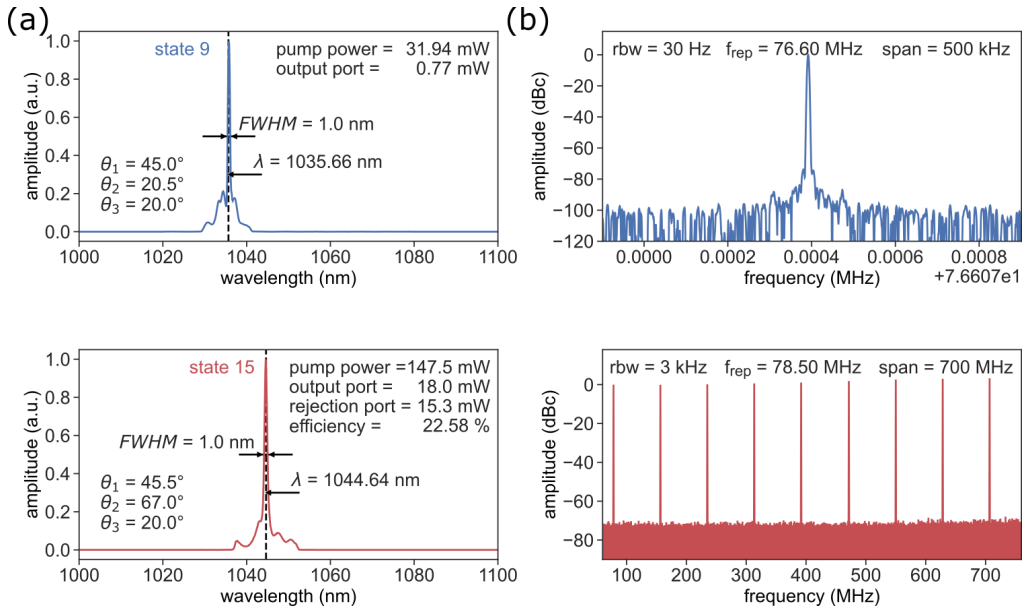

Figure 4.6: Spectra and repetition rates. Spectral shapes of the max positive net-GDD regime with the FWHM, the centroid wavelength, and characteristic powers, where the θ_i's are the corresponding waveplate angles (a). The f_{rep} recorded with a span of 700 MHz and a resolution-bandwidth of 3 kHz (b).

change from CW lasing to pulsed lasing. After mode-locking, clean mode-locking was reached by reducing the pump power close to the CW threshold alignment. Figure 4.7 also shows a zoom into the pump power range where clean mode-locking exists. In the positive net-GDD regime (Fig. 4.7c, d), an entirely different mode-locking behavior exists. Here, the angle θ_1 of the $\lambda/2$ waveplate was changed so that higher cavity losses occur, resulting in a lower gradient in the laser slope during CW lasing and a significant change in intra-cavity power when changing from CW to pulsed operation. An advantage of jumping directly to the clean mode-locked state is that the creation of harmful Q-switched pulses can be mostly avoided, as these can damage the laser components. Another significant behavior is that further overpumping interrupts pulsed lasing and subsequent reduction of the pump power resumes mode-locking. This behavior results from the strong influence of the Kerr effect in the fiber. The max positive net-GDD regime (Fig. 4.7e, f) shows similar mode-locking behavior to the negative net-GDD regime (Fig. 4.7a, b), except that clean mode-locking, occurs at higher output power.
The near-zero net-GDD regime has no characteristic laser slope, see Fig. 4.8. The laser slopes show a transition between the negative and positive net-GDD regime behavior. State 5 starts directly in clean mode-locking, and by a further increase of the pump power, mode-locking does not break up. At state 14, on the other hand, the pulsed operation stops when the pump power is further increased. In state 14, a second clean mode-locking state also occurs, which is reached by decreasing the pump power from the higher power state, see Fig. 4.8f. This behavior results from the large differences of

Die approbierte gedruckte Originalversion dieser Diplomarbeit ist an der TU Wien Bibliothek verfügbar.
The approved original version of this thesis is available in print at TU Wien Bibliothek.
TU Bibliothek Your knowledge hub WIEN

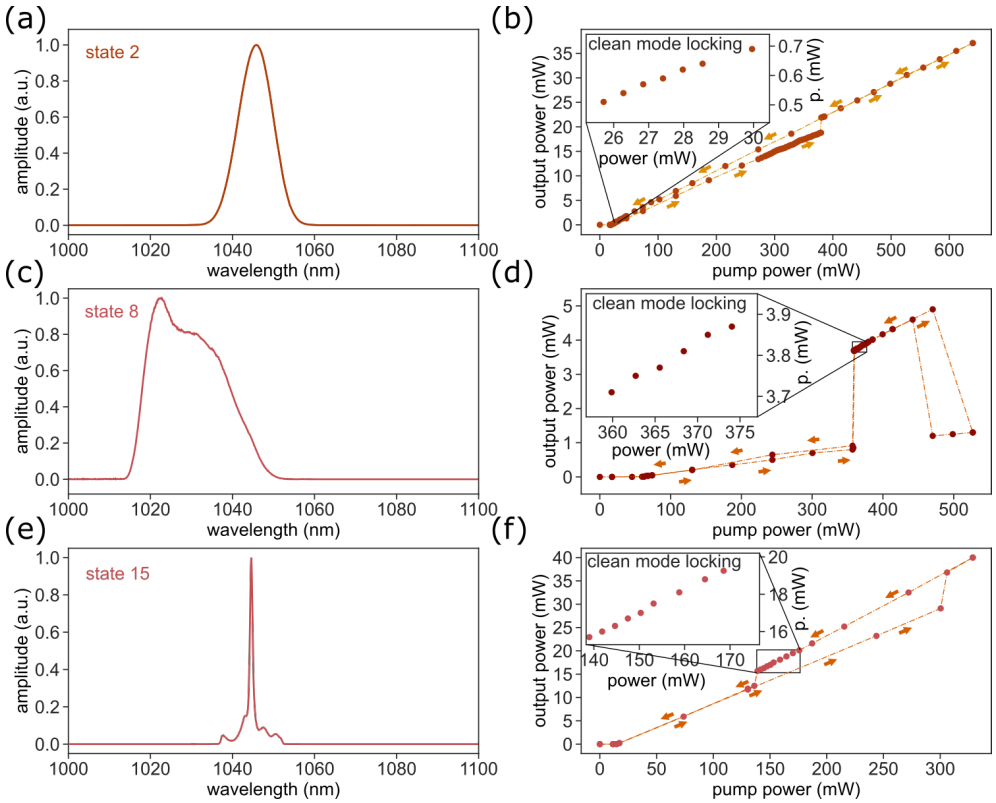

Figure 4.7: Characteristic spectra and laser slopes. Characteristic spectra for the negative, near-zero and max positive net-GDD regime (a). Characteristic laser slopes of the corresponding spectra in (a) with a zoom into the clean mode-locking range (b).

Die approbierte gedruckte Originalversion dieser Diplomarbeit ist an der TU Wien Bibliothek verfügbar.
The approved original version of this thesis is available in print at TU Wien Bibliothek.
TU Bibliothek Your knowledge hub WIEN

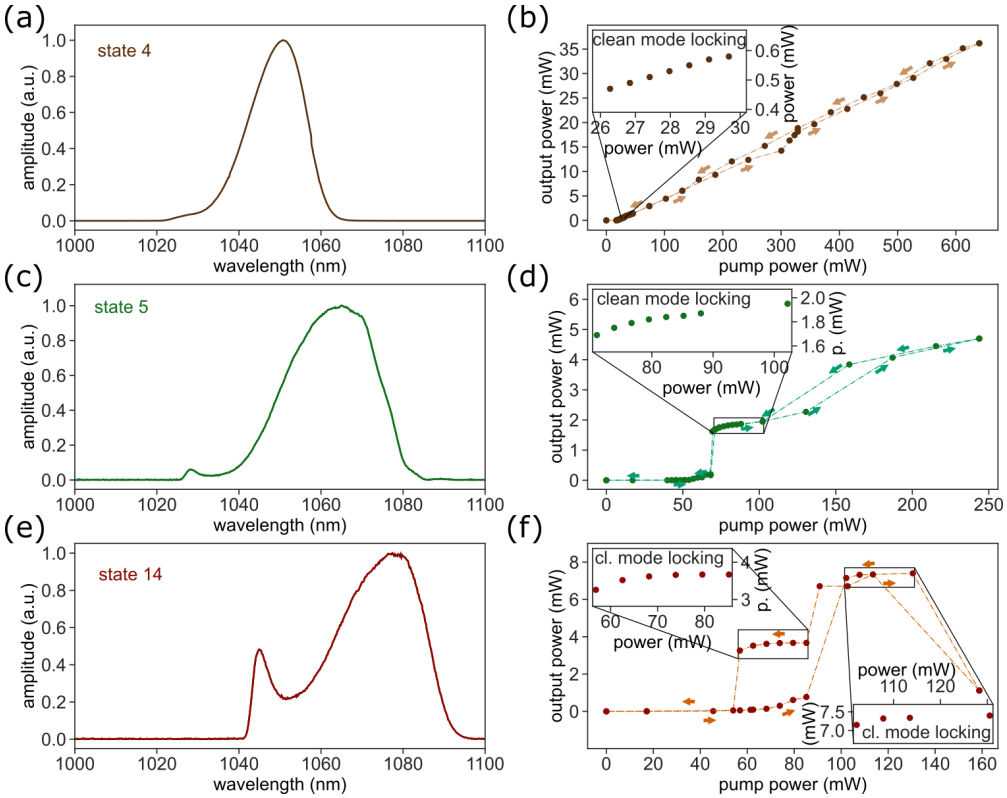

Figure 4.8: Characteristic spectra and laser slopes. Spectra in the near-zero net-GDD (a). Laser slopes of the corresponding spectra in (a) with a zoom into the clean mode-locking range (b).

Die approbierte gedruckte Originalversion dieser Diplomarbeit ist an der TU Wien Bibliothek verfügbar.
The approved original version of this thesis is available in print at TU Wien Bibliothek.

the waveplate angles between the negative and positive net-GDD regimes, which do not allow a continuous transition between these regimes. Since pulse lasing in our setup has a lower energy state than CW lasing, the system tends to maintain the pulse solution of the negative net-GDD regime. Figure 4.1 shows that for higher wavelengths, the net-GDD decreases, which leads to a shift of the central wavelength to higher wavelengths.

4.3 Knox-measurement

The main part of the characterization consisted in measuring the net-GDD of the different mode-locking states. To determinate the net-GDD, I used the technique invented by Knox [30]. Using the Knox-measurement I generated a net-GDD map, which shown in Figure 4.1. However, when interpreting the presented GDD-map, the limitations of the Knox method must be taken into account. In this section, we will discuss the various influences of the different mode-locking regimes based on these limitations.
I am starting with the negative net-GDD regime, which contains state 1–3, 10 and 11. Figure 4.9 shows the measured data. The plotted angular frequencies show a small deviation from the quadratic fit, which we attribute to neglecting the fourth-order dispersion in the analysis of the Knox-measurement, as described in Sec. 2.3.3. Comparing the plotted Spectra with the corresponding fit residuals shows that a smooth spectral shape decreases the deviations. It was observed that a slight variation of the pump power can smoothen the spectrum such that the fits improve.
To demonstrate the small influence of a power variation, we measured the first two states with varying pump powers of 200 mA, 300 mA and 400 mA, as shown in Fig. 4.10. Here again, the difference in smoothness of the spectra explains the slight deviations of the net-GDD slopes. We have made these measurements with almost the same waveplate angles. In contrast, the net-GDD measurements of state 10 and 11 lead to a different gradient of the curve, due to the different waveplate angles. Figure 4.1 shows the deviation in the net-GDD curve between lasers 1 and laser 2 at grating separations of 12.1 mm and 11.1 mm. The mean net-GDD distance between the 12.1 mm and 11.1 mm grating distance net-GDD curves also deviates from the calculated net-GDD value of the grating compressor with 1 mm separation. This determined GDD value corresponds more precisely to the gap between state 1 and 2, where the waveplate angles do not change. This behavior shows the influence of the waveplate angles on the net-GDD.
The spectra of the net-GDD measurement at grating separations of 9.1 mm and 8.1 mm show a significant change in spectral shape indicating a transition of the mode-locking state, see Fig. 4.11. Additionally, the measured data points exhibit a systematic deviation from the quadratic fit function for both states, which is clearly visible in the resdiual plots. Nevertheless, the error is of the same order of magnitude as the error in the negative net-GDD regime. It is worth mentioning that we recorded the net-GDD curve for the grating separation of 9.1 mm in one pass. The change in the spectra occured continuously, as can be seen in Fig. 4.11a, b. Whereas at 8.1 mm grating distance, the pulse lasing stopped during the measurement (Fig. 4.11c, d). The spectra at shorter wavelengths required a restart with higher pump power and a repositioning of the wave-

Die approbierte gedruckte Originalversion dieser Diplomarbeit ist an der TU Wien Bibliothek verfügbar.
The approved original version of this thesis is available in print at TU Wien Bibliothek.
TU Bibliothek Your knowledge hub WIEN

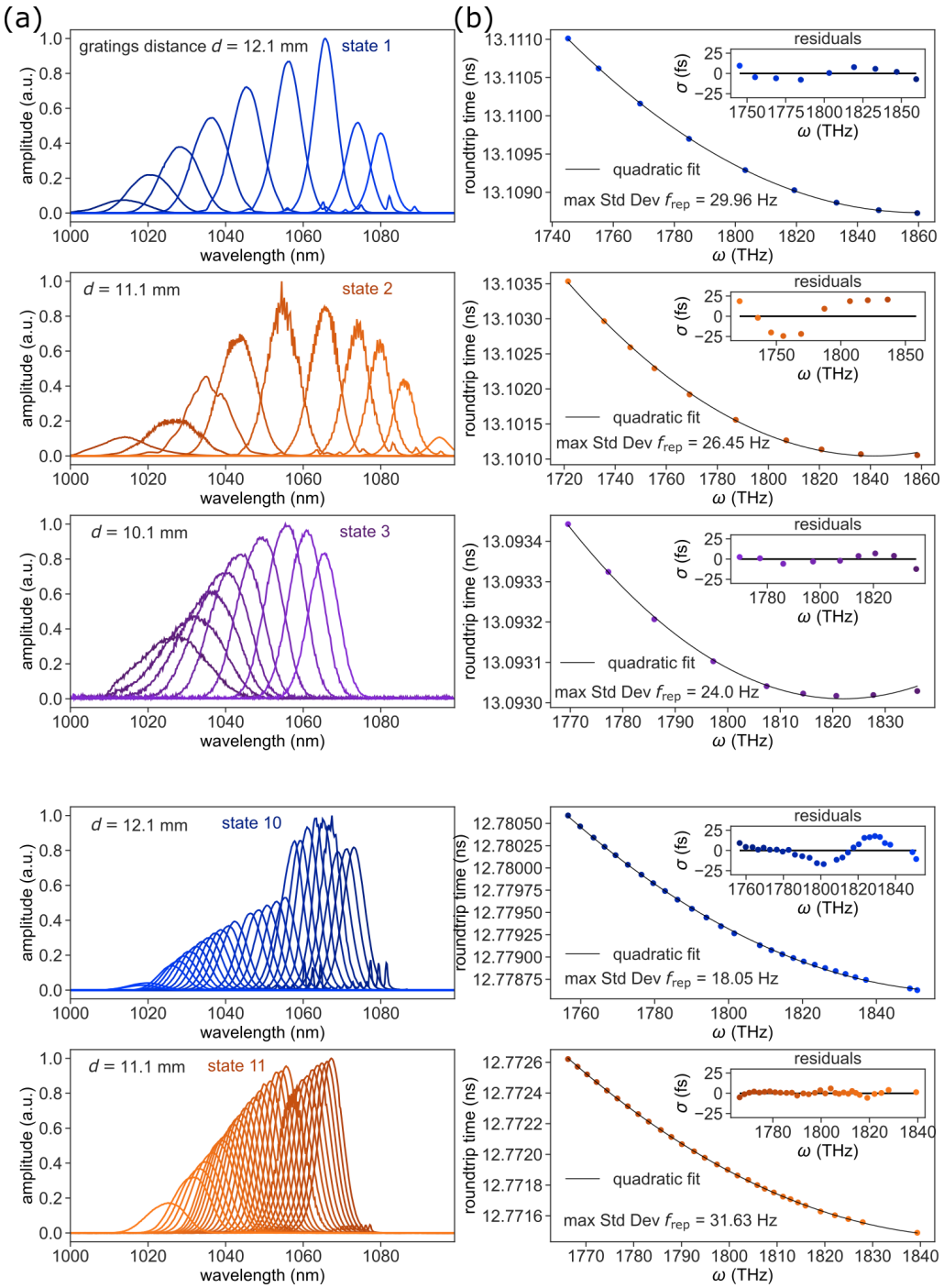

Figure 4.9: Knox-measurements for clean mode-locking states with a 12.1 mm, 11.1 mm and 10.1 mm grating separation. From the recorded spectra (a) the centroid wavelengths are extracted. After conversion into angular frequency they are plotted against the round-trip time (b). A quadratic fit to the data including residuals is shown.

Die approbierte gedruckte Originalversion dieser Diplomarbeit ist an der TU Wien Bibliothek verfügbar.
The approved original version of this thesis is available in print at TU Wien Bibliothek.

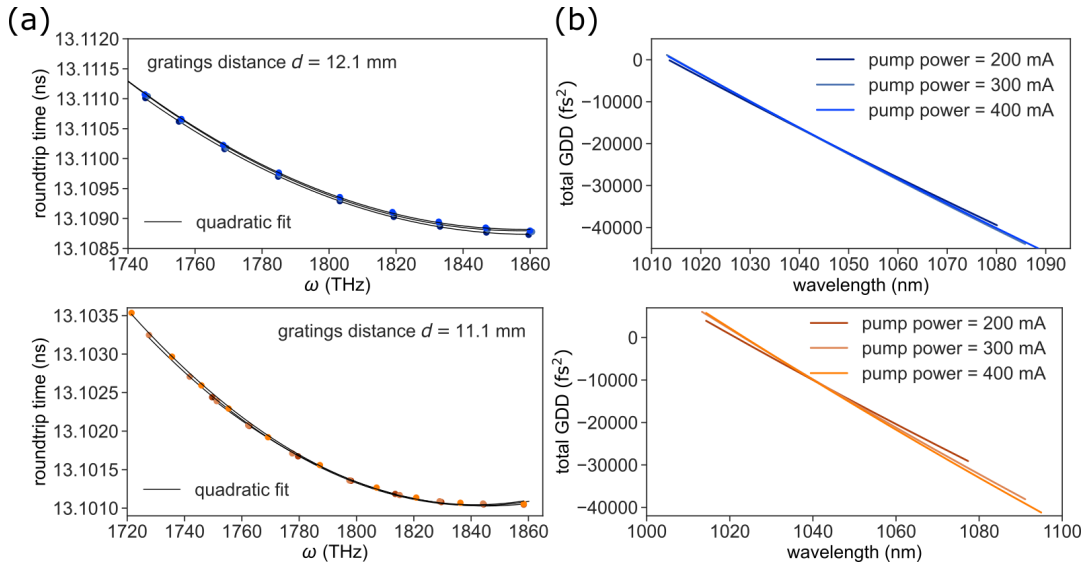

Figure 4.10: Knox-measurement data sets at 12.1 mm and 11.1 mm grating separation with various pump powers (a). Net-GDD curves of the corresponding data sets of (b).

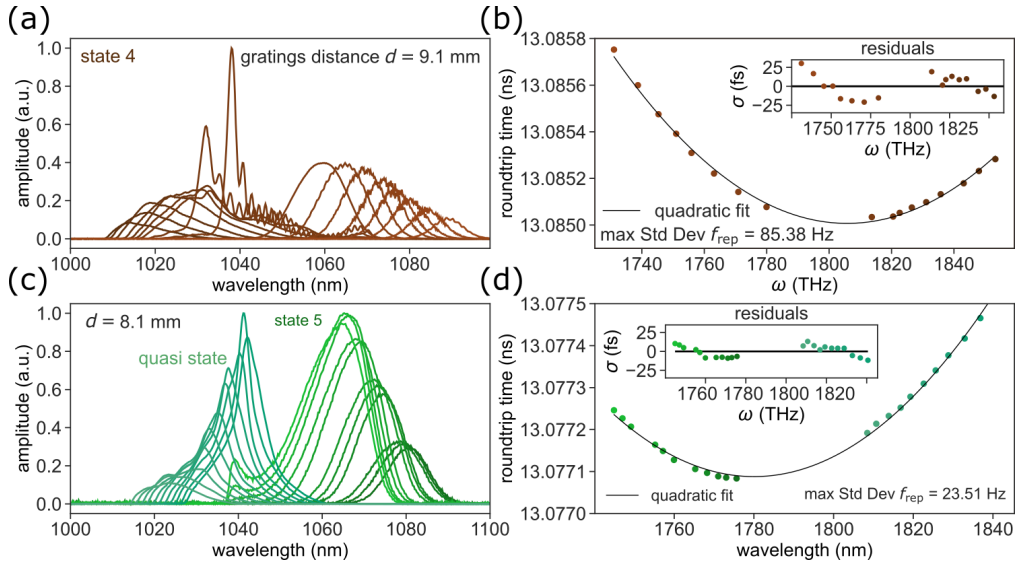

Figure 4.11: Knox-measurements for clean mode-locking states with a 9.1 mm, and 10.1 mm grating separation and uniform waveplate angles. From the recorded spectra (a, c) the centroid wavelengths are extracted. After conversion into angular frequency they are plotted against the round-trip time (c, d). A quadratic fit to the data including residuals is shown.

Die approbierte gedruckte Originalversion dieser Diplomarbeit ist an der TU Wien Bibliothek verfügbar.
The approved original version of this thesis is available in print at TU Wien Bibliothek.
TU Bibliothek Your knowledge hub WIEN

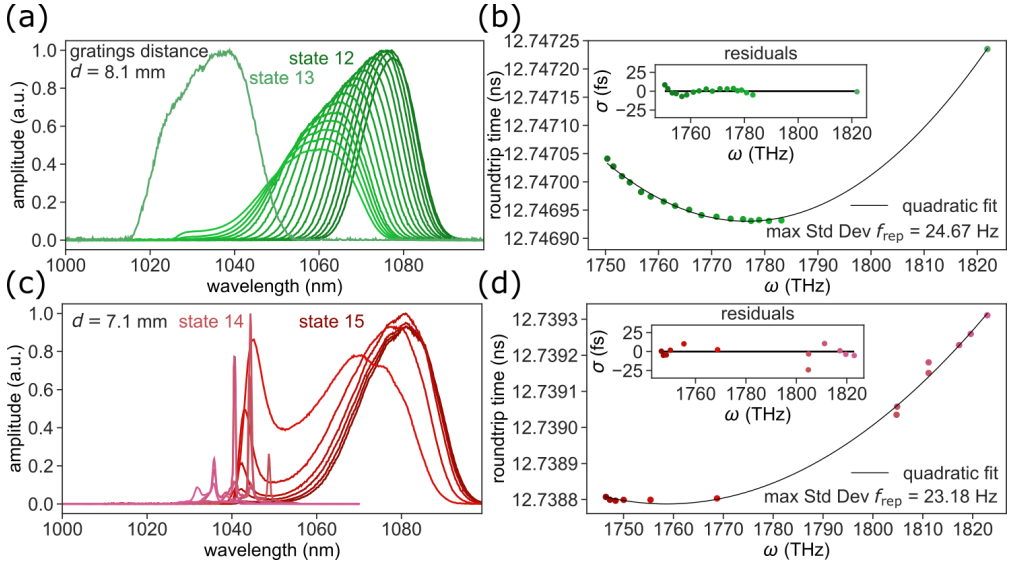

Figure 4.12: Knox-measurements for clean mode-locking states with a 9.1 mm and 10.1 mm grating separation and changing waveplate angles. From the recorded spectra (a, c) the centroid wavelengths are extracted. After conversion into angular frequency they are plotted against the round-trip time (b, d). A quadratic fit to the data including residuals is shown.

length filtering slit, but without variation of the waveplate angles. Furthermore, this state was only found with the slit in place (Fig. 2.9) and is called quasi state.
For the net-GDD measurement of laser 2 with grating separations of 8.1 mm and 7.1 mm, we used entirely different parameters for the different clean mode-locking states. For instance, we extended the data set from the Knox-measurement at state 12 by the single data pair from the operating point at state 13, as can be seen in the top panel of Fig. 4.12. State 13 has an output power of about 100 mW, and therefore a separate Knox-measurement is too risky because of possible laser damage. For the GDD estimation of state 13, an extension of the data set was necessary. The combination of the net-GDD measurement of states 14 and 15 (bottom panel of Fig. 4.12) leads to an adequate data set, whereas due to the short shifting-range of the slit, each data set itself does not lead to a useful result.
However, the combination of net-GDD measurement data sets of different clean mode-locking states is not always suitable. Therefore, combinations of different data sets require a plausibility check. The combination of the measured data of states 12 and 13 results in results in a good quality fit. In contrast, the data set of state 5 with the quasi state replaced by state 6 leads to unphysical results, see Fig. 4.13. Figure 4.13 shows the significant differences between possible combinations based on state 5. The strong deviation of one data point of state 6 originates from the different laser parameters, and especially from the different values of the wave plate angles. For the slope of the net-GDD of state 6 a separate net-GDD measurement is necessary, which was not performed,

Die approbierte gedruckte Originalversion dieser Diplomarbeit ist an der TU Wien Bibliothek verfügbar.
The approved original version of this thesis is available in print at TU Wien Bibliothek.
TU Bibliothek Your knowledge hub WIEN

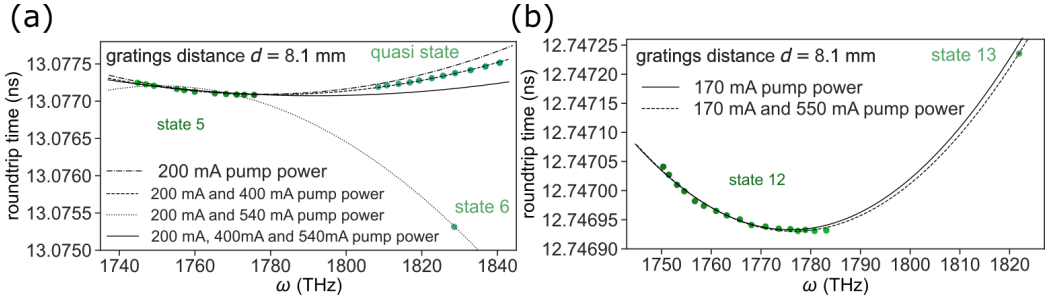

Figure 4.13: Different combinations of the data sets for a group delay at 8.1 mm grating separation of laser 1 and laser 2 as a function of the frequency (a, b), where the combinations are given by the pump powers of the states.

because the high pump power of this state leads to much stronger Q-switch pulses and thus to a higher risk of damage. The uncertainties of the net-GDD of state 6 and state 7 are illustrated in the net-GDD map by a larger marker for the datapoint.
Finally, a summary of the net GDD, wavelength, pump power and output power ranges associated with the four net-GDD regimes and their efficiency are listed in Tab. 4.1.

Table 4.1: Summarize of the net-GDD regimes and there characteristics

Net-GDD regime	Net-GDD range (ps^2)	Wavelengths range (nm)	Pump power (mW)	Output power (mW)	Effcy.
Negative	−0.03 to −0.005	140 to 159	27 to 34	0.5 to 3	∼ 15%
Near-zero	−0.005 to 0	149 to 173	30 to 100	0.6 to 4	∼ 30%
Positive	0.01 to 0.022	128 to 135	250 to 500	4 to 190	∼ 60%
Max pos.	0.01 to 0.03	135 to 145	30 to 150	0.8 to 18	∼ 20%

Die approbierte gedruckte Originalversion dieser Diplomarbeit ist an der TU Wien Bibliothek verfügbar.
The approved original version of this thesis is available in print at TU Wien Bibliothek.

5 Summary and Outlook

In summary, we presented a dispersion dependent laser characterization of an all-polarisation-maintaining, nonlinear amplifying loop mirror mode-locked fiber laser. Clean mode-locking operation has been demonstrated in various dispersion regimes, by scanning the intracavity group delay dispersion via a grating compressor inside the lasers resonator. The flexible laser design allowed for finding various mode-locking states. We have mapped the clean mode states in a net-GDD map, which shows all recorded operation points. The net cavity dispersion was not only calculated from the dispersion data of the components but was quantified using the technique of Knox. For the laser presented in this work, a lower and upper group delay dispersion limit for stable mode-locking operation was observed and verified. Between the dispersion limits, four characteristic operation behaviors could be observed. For the net negative dispersion range of $-30\,000\,\mathrm{fs}^2$ to $-5000\,\mathrm{fs}^2$, $sech^2$ shaped optical spectra were observed. For all operation states within this regime the laser operates with nearly the same wave plate positions, end mirror alignment, and pump power. For the operation point with the highest negative dispersion value, Kelly sidebands have been observed. For the dispersion regime close to zero, from $-5000\,\mathrm{fs}^2$ to $0\,\mathrm{fs}^2$, the pulse spectra exhibit a characteristic side peak towards the zero dispersion point. In this regime, different waveplate positions and end mirror alignment are needed for every state. The near-zero net-GDD regime requires significantly more pump power than the negative net-GDD region. For the positive dispersion regime in the range of $10\,000\,\mathrm{fs}^2$ to $22\,000\,\mathrm{fs}^2$, we notice a further increase in the required pump power. The reason for this is that clean mode-locking in the positive net-GDD regime requires much higher cavity losses. These higher losses lead to a starting behavior, which makes the laser directly jump into the clean mode-locking state and the intracavity field can carry much more power than the other regime states. The max-positive net-GDD regime represents the upper limit of the net GDD, marked by signicantly small FWHMs of the spectrum.

The analysis presented here will work as a starting point to develop an all-polarisation-maintaining seed laser for frequency comb spectroscopy in the mid-IR frequency range. The fundamental limitation of the spectroscopic resolution, which can be achieved with a frequency comb, is given by the linewidth of the comb teeth. This linewidth, on the other hand, is depending on the stability of f_{rep} and f_{CEO}. The stabilization of f_{rep} and f_{CEO} is a challenging task, however, it is of great importance too that the noise of the free-running laser used is already as low as possible. Therefore, a comprehensive noise study, including the relative intensity noise (RIN) and the phase noise of f_{rep} and f_{CEO}, of the different operation states is essential for the selection of the final most suitable operation state.

The work presented here was extended in the CDL-MIR lab. In addition to the mea-

Die approbierte gedruckte Originalversion dieser Diplomarbeit ist an der TU Wien Bibliothek verfügbar.
The approved original version of this thesis is available in print at TU Wien Bibliothek.
TU Bibliothek Your knowledge hub WIEN

surements shown in this thesis, RIN measurements, phase noise and free running f_{CEO} linewidth measurements were performed for all states. The full characterization of the figure-9 laser built during this theses was recently published in [24].

Die approbierte gedruckte Originalversion dieser Diplomarbeit ist an der TU Wien Bibliothek verfügbar.
The approved original version of this thesis is available in print at TU Wien Bibliothek.

6 Appendix

Table 6.1: Laser Components

Component	Description
Pump diode	Thorlabs BL976-PAG900
Pump diode controller	Thorlabs CLD1015
Pump isolator	AFR HPMI-976-02-N-B-QF-1-C
Wavelengtah division	AFR PMFWDM-9806-N-B-Q
Single mode PM fiber	Corning PANDA PM980
Gain fiber	CorActive Yb-401-PM
Polarization beam combiner cube with integrated collimation lens (PBCC)	AFR Semi-PBCC-03-09-N-B-Q)
Faraday rotator	EOT HP-05-R-1030
$\lambda/2$ waveplate	Thorlabs WPH05M-1030
$\lambda/4$ waveplate	Thorlabs WPH05M-1030
Polarization beam splitter	Thorlabs PBS103
Gratings	LightSmyth T-1000-1040-3212-94
End mirror	Thorlabs PF10-03-P01

Table 6.2: Measuring Instruments

Device	Description
Radiofrequency (RF) analyzer with a 5 GHz photo diode	Keysight PXA N9030B Thorlabs DET08 InGaAs
Optical spectrum analyzer (OSA)	Ando AQ6315A
Powermeter	Thorlabs PM 100 A
Beamprofiler	Newport LBP2-VIS2

Die approbierte gedruckte Originalversion dieser Diplomarbeit ist an der TU Wien Bibliothek verfügbar.
The approved original version of this thesis is available in print at TU Wien Bibliothek.
TU Bibliothek Your knowledge hub WIEN

7 Acknowledgments

The list of people that have contributed in helping me finish this thesis is long and I probably will not be able to get it complete here. However, I would like to particularly mention a few that played an important role.
First of all, I would like to thank Oliver Heckl with his team Georg Winkler, Aline Mayer Jakob Fellinger and Lukas Perner for offering me the opportunity to do my thesis on such an interesting project, like fiber lasers. With their untiring support and guidance they helped me to complete this thesis.
Transitioning to a more personal level, I would like to thank all my fellow students at the TU Wien. You have indisputably made the study time of my physics studies an unforgettable time. For productive discussions about physics and life in general, I would like to thank: Thomas Madlener, Lukas Semmelrock, Matthias Müllner, Jakob Necker, Michael Wallner, Johannes Brandstetter and Jakob Fellinger.
I would like to thank as well all my friends from my home village for their support and encouragement during my studies. Thanks guys.
And finally, the ones with the possible largest share towards my success so far, my family: Thank You Mama, Thank You Papa, Thank You Jasmin, Thank You Bernhard and Marlene. For your everlasting support in every area of life and in general just for being there whenever I need you.

Die approbierte gedruckte Originalversion dieser Diplomarbeit ist an der TU Wien Bibliothek verfügbar.
The approved original version of this thesis is available in print at TU Wien Bibliothek.
TU Bibliothek Your knowledge hub WIEN

Bibliography

[1] Albert Einstein. "Strahlungs-emission und-absorption nach der Quantentheorie". In: Verh. Deutsch. Phys. Gesell. 18 (1916), pp. 318–323.

[2] Rüdiger Paschotta. Guide to Lasers, Hobarts. URL: https://hobarts.com/guide-to-lasers (visited on 12/05/2019).

[3] R. Gordon Gould. "The LASER, Light Amplification by Stimulated Emission of Radiation". In: Michigan: The Ann Arbor Conference on Optical Pumping, the University of Michigan, 1959, p. 128.

[4] Jeff Hecht. "Beam: The Race to Make the Laser". In: Opt. Photon. News 16.7 (July 2005), pp. 24–29. DOI: 10.1364/OPN.16.7.000024. URL: http://www.osa-opn.org/abstract.cfm?URI=opn-16-7-24.

[5] A. Javan, W. R. Bennett, and D. R. Herriott. "Population Inversion and Continuous Optical Maser Oscillation in a Gas Discharge Containing a He-Ne Mixture". In: Phys. Rev. Lett. 6 (3 Feb. 1961), pp. 106–110. DOI: 10.1103/PhysRevLett.6.106. URL: https://link.aps.org/doi/10.1103/PhysRevLett.6.106.

[6] John L. Hall. "Nobel Lecture: Defining and measuring optical frequencies". In: Rev. Mod. Phys. 78 (4 Nov. 2006), pp. 1279–1295. DOI: 10.1103/RevModPhys.78.1279. URL: https://link.aps.org/doi/10.1103/RevModPhys.78.1279.

[7] Rüdiger Paschotta. Frequency Combs, RP Photonics Encyclopedia. URL: https://www.rp-photonics.com/frequency%7B%5C_%7Dcombs.html (visited on 12/05/2019).

[8] Rüdiger Paschotta. Mode Locking, RP Photonics Encyclopedia. URL: https://www.rp-photonics.com/mode%7B%5C_%7Dlocking.html (visited on 12/05/2019).

[9] Rüdiger Paschotta. Mode Locking Devices, RP Photonics Encyclopedia. URL: https://www.rp-photonics.com/mode%7B%5C_%7Dlocking%7B%5C_%7Ddevices.html (visited on 12/05/2019).

[10] Rüdiger Paschotta. Solid-state Lasers, RP Photonics Encyclopedia. URL: https://www.rp-photonics.com/solid%7B%5C_%7Dstate%7B%5C_%7Dlasers.html (visited on 12/05/2019).

[11] Rüdiger Paschotta. Fiber Lasers, RP Photonics Encyclopedia. URL: https://www.rp-photonics.com/fiber%7B%5C_%7Dlasers.html (visited on 12/05/2019).

[12] Rüdiger Paschotta. Waveguide Lasers, RP Photonics Encyclopedia. URL: https://www.rp-photonics.com/waveguide%7B%5C_%7Dlasers.html?s=ak (visited on 12/05/2019).

Die approbierte gedruckte Originalversion dieser Diplomarbeit ist an der TU Wien Bibliothek verfügbar.
The approved original version of this thesis is available in print at TU Wien Bibliothek.
TU Bibliothek Your knowledge hub WIEN

[13] Rüdiger Paschotta. Microchip Lasers, RP Photonics Encyclopedia. URL: https://www.rp-photonics.com/microchip%7B%5C_%7Dlasers.html?s=ak (visited on 12/05/2019).

[14] Rüdiger Paschotta. Semiconductor Saturable Absorber Mirrors, RP Photonics Encyclopedia. URL: https://www.rp-photonics.com/semiconductor%7B%5C_%7Dsaturable%7B%5C_%7Dabsorber%7B%5C_%7Dmirrors.html (visited on 12/05/2019).

[15] Rüdiger Paschotta. Kerr Lens, RP Photonics Encyclopedia. URL: https://www.rp-photonics.com/kerr%7B%5C_%7Dlens.html?s=ak (visited on 12/05/2019).

[16] Rüdiger Paschotta. Gain Media, RP Photonics Encyclopedia. URL: https://www.rp-photonics.com/gain%7B%5C_%7Dmedia.html?s=ak (visited on 12/05/2019).

[17] Rüdiger Paschotta. Nonlinear Frequency Conversion, RP Photonics Encyclopedia. URL: https://www.rp-photonics.com/nonlinear%7B%5C_%7Dfrequency%7B%5C_%7Dconversion.html?s=ak (visited on 12/05/2019).

[18] Wolfgang Demtröder. Laserspektroskopie 2. 6th ed. Springer, 2013, p. 273.

[19] Andy Chong, Logan G. Wright, and Frank W. Wise. "Ultrafast fiber lasers based on self-similar pulse evolution: A review of current progress". In: Reports on Progress in Physics 78.11 (2015). ISSN: 00344885. DOI: 10.1088/0034-4885/78/11/113901.

[20] M. E. Fermann et al. "Nonlinear amplifying loop mirror". In: Optics Letters 15.13 (1990), p. 752. ISSN: 0146-9592. DOI: 10.1364/ol.15.000752.

[21] Wolfgang Hänsel et al. "All polarization-maintaining fiber laser architecture for robust femtosecond pulse generation". In: Applied Physics B: Lasers and Optics 123.1 (2017), pp. 1–6. ISSN: 09462171. DOI: 10.1007/s00340-016-6598-2.

[22] Rüdiger Paschotta. Polarization-maintaining Fibers, RP Photonics Encyclopedia. URL: https://www.rp-photonics.com/polarization%7B%5C_%7Dmaintaining%7B%5C_%7Dfibers.html?s=ak (visited on 12/05/2019).

[23] Rüdiger Paschotta. Group Delay Dispersion, RP Photonics Encyclopedia. (Visited on 12/05/2019).

[24] Aline S. Mayer et al. "Flexible all-PM NALM Yb:fiber laser design for frequency comb applications: operation regimes and their noise properties". In: Opt. Express 28.13 (June 2020), pp. 18946–18968. DOI: 10.1364/OE.394543. URL: http://www.opticsexpress.org/abstract.cfm?URI=oe-28-13-18946.

[25] Rüdiger Paschotta. Chromatic Dispersion, RP Photonics Encyclopedia.

[26] Rüdiger Paschotta. Sellmeier formula, RP Photonics Encyclopedia. URL: https://www.rp-photonics.com/sellmeier_formula.html (visited on 04/05/2020).

[27] Mikhail N. Polyanskiy. Refractive index database. https://refractiveindex.info. Accessed on 2020-04-05.

[28] Jungwon Kim and Youjian Song. "Ultralow-noise mode-locked fiber lasers and frequency combs: principles, status, and applications". In: Adv. Opt. Photon. 8.3 (Sept. 2016), pp. 465–540. DOI: 10.1364/AOP.8.000465. URL: http://aop.osa.org/abstract.cfm?URI=aop-8-3-465.

Die approbierte gedruckte Originalversion dieser Diplomarbeit ist an der TU Wien Bibliothek verfügbar.
The approved original version of this thesis is available in print at TU Wien Bibliothek.
TU Bibliothek Your knowledge hub WIEN

[29] Rüdiger Paschotta. Peak power, RP Photonics Encyclopedia. URL: https://www.rp-photonics.com/peak_power.html (visited on 04/05/2020).

[30] W. H. Knox. "In situ measurement of complete intracavity dispersion in an operating Ti:sapphire femtosecond laser". In: Optics Letters 17.7 (1992), p. 514. ISSN: 0146-9592. DOI: 10.1364/ol.17.000514.

Die approbierte gedruckte Originalversion dieser Diplomarbeit ist an der TU Wien Bibliothek verfügbar.
The approved original version of this thesis is available in print at TU Wien Bibliothek.